Utrecht University

INORGANIC CHEMISTRY & CATALYSIS

Tuning the Size of Colloidal Ni Nanoparticles for CO_2 Hydrogenation Catalysis

Master's Thesis

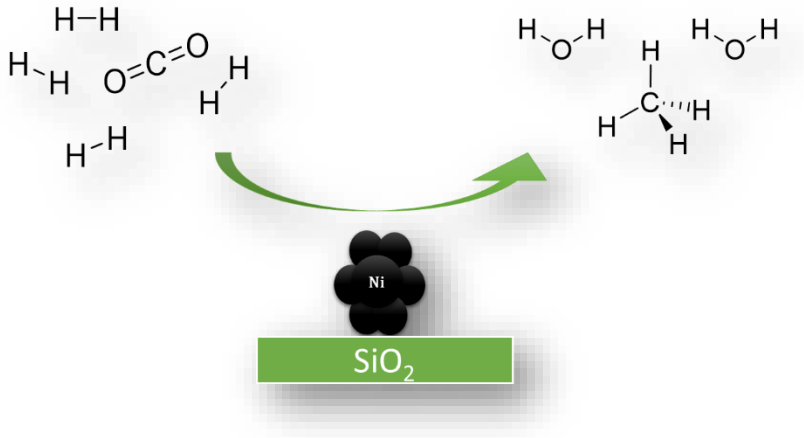

Metin Sen, BASc

Supervisors:

Bram Kappé, MSc (Daily supervisor)

Dr. Matteo Monai (First examiner)

Dr. Ward van der Stam (Second examiner)

5 February 2023

Layman's abstract

Climate change is a pressing problem of this century and the coming centuries due to the high emissions of greenhouse gases (CO_2, CH_4 and N_2O). A lot of ideas and solutions are being explored to tackle this problem. The solution should be chosen very wisely to get high efficiency. An efficient solution could be converting the main responsible greenhouse gas, carbon dioxide (CO_2), to valuable products, such as the main gas methane, in natural gas. By converting CO_2 to useful products, the CO_2 amount in the atmosphere will decrease, and the global temperature could be slowed down.

CO_2 can be converted using metal catalysts like ruthenium, cobalt and nickel. Nickel stands out from these metals because of its availability in large quantities, low price and efficient conversion of CO_2 to methane. The conversion occurs at the catalyst's surface and is therefore, sensitive to the catalyst's surface. CO_2 conversion over nickel catalysts prefers nanoparticles with 2.5 nm because of the high amount of active sites. Therefore, it is important to have more nickel nanoparticles with an optimal size of 2.5 nm in the catalysts to get a high conversion to methane.

This project shows a method (colloidal synthesis) to prepare small nickel nanoparticles of similar size (monodisperse). Different parameters were changed during the synthesis to control the nickel nanoparticle size. It yielded nickel nanoparticles ranging from 1.4 nm to 6.6 nm. Five catalyst samples with different nickel particle sizes were prepared on silica and tested in CO_2 conversion experiments. Here, infrared spectroscopy was used to detect the methane gas in products. The results showed that five samples were all active in CO_2 conversion to methane. However, the obtained activity trend was different with maximum activity around 4.0 nm than the reported activity trend in the literature. Further research is needed to draw an accurate conclusion about the activity of these prepared nickel nanoparticles. In the end, a new method was developed to prepare small and monodisperse nickel nanoparticles for CO_2 conversion.

Abstract

Increasing demand for environmentally friendly produced fuels caused the interest in converting CO_2 to useful products such as methane over Ni-based catalysts. Because the CO_2 conversion (hydrogenation) over Ni catalysts is structure sensitive, it became essential to understand the role of the particle size and shape. It has been reported that silica-supported Ni nanoparticles around 2.5 nm particle size have the maximum catalytic activity.[1,2] However, synthesizing small and monodisperse Ni nanoparticles (NP) below 3.0 nm was challenging with the ability to simultaneously deposit Ni NPs from the same batch on separate supports. Therefore, the ability to synthesize monodisperse Ni NPs around 2.5 nm is necessary for CO_2 hydrogenation catalysis. The colloidal approach provides the possibility for high control in the particle size distribution by varying the reactants and reaction temperature during the synthesis of nanoparticles. However, ligand removal forms a well-known obstacle in colloidal synthesis. When the ligands are not appropriately removed, metal NPs could be inactive in the catalysis because of surface blockage.

This study shows a new synthesis approach for colloidal Ni NPs, including ligand removal and deposition on the silica support for CO_2 hydrogenation catalysis. Small colloidal Ni NPs were synthesized using the hot injection method. The Ni NP sizes were between 1.4 nm and 6.6 nm with a standard deviation of 13-30 %. The particle size was controlled by changing the ligands, reaction temperature and reactant ratios. Subsequently, the colloidal Ni NPs were deposited on the silica support and the ligands were removed by Meerwein's reagent alkylation, as proven by operando FT-IR studies. The remaining ethyl groups from Meerwein's reagent were removed during the

catalyst's reduction. In the last part of this project, seven silica-supported Ni catalysts were prepared for CO_2 hydrogenation catalysis and studied using operando FT-IR. Five Meerwein's reagent-treated catalysts were highly active compared to a commercial catalyst, while untreated samples were not active in CO_2 hydrogenation catalysis. Here, our colloidal approach provides a new synthesis method to synthesize Ni nanoparticles for CO_2 hydrogenation catalysis that are smaller than reported, without P-containing ligands, monodisperse and catalytic active, and that can be deposited on separate supports simultaneously

Contents

1. Introduction

The well-known evidence for climate change is the global increase in temperature and sea level, and the meltdown of the ice sheets caused mainly by greenhouse gasses (CO_2, CH_4 and other gasses).[3] There are several solutions to reduce greenhouse gas emissions. Renewable energy (solar and wind), nuclear powers and biomass are solutions which are in use. Besides these solutions, as an alternative solution, the use of CO_2 as an energy feedstock could help to slow CO_2 emissions.

The importance of these methods was understood and got the attention of scientists.[4] CO_2 hydrogenation to methane and other hydrocarbons[5] has gained interest particularly.[6] CO_2 could be reduced by using photocatalysis,[7] electrocatalysis,[8] and thermal catalysis. CO_2 hydrogenation over metal-based catalysts using H_2 from renewable energy sources is seen as a promising method to convert CO_2 to hydrocarbons.[6,9]

Different metal-based catalysts are researched; among them, Ni,[10,11] Ru,[12] Rh,[13] Co,[11] and Pd,[14] are the metals catalysts whereby CH_4 is formed. Using other metal-based catalysts resulted in other hydrocarbon products (methanol,[15] dimethyl ether[16] and light olefins[17]). Several successful methods have been developed and used to produce metal nanoparticles for heterogeneous catalysts from noble metals (Ru, Rh, Pd). The large specific area is an advantageous property of nanoparticles, which is desirable for catalytic reactions.[18,19] Ni-based catalysts are more of interest in the industry because of their high CH_4 selectivity, wide availability, and low cost than noble metals (Ru, Rh, Pd), while noble metal catalysts are more active than nickel catalysts.[6]

For the first time, CO_2 methanation over a nickel-based catalyst was described by Paul Sabatier in 1902, which is now known as the Sabatier reaction in his honor.[20] The Sabatier reaction has gained the interest of scientists again with the idea of developing new strategies for reducing CO_2 emissions. Since 1902, a lot of research has been done on catalysis reactions over Ni-based catalysts to convert CO_2. The works by Vogt and co-workers[1,21] and other studies[2] show that CO_2 hydrogenation catalysis over Ni-based catalysts is a structure sensitivity reaction. Meaning is that CO_2 hydrogenation catalysis over Ni-based catalyst is particle shape and size dependent with an optimum activity of Ni nanoparticle with a specific particle size (Type I).

The colloidal synthesis route is one of the most promising methods to synthesize supported size-controlled Ni NPs.[10] During the colloidal synthesis, the shape, size and composition could be controlled. Herein, two main challenges are crucial to getting the desired product. The first challenge is nanoparticle size control and the second is the removal of the available ligands after the deposition of nanoparticles on the support. Multiple studies have been conducted to control the size of Ni particles by adjusting reaction temperature and ligand. Unfortunately, the reported colloidal studies could not show a procedure to synthesize nanoparticles smaller than 3.0 nm.[10,22–24] Vrijburg and co-workers have reported how to synthesize colloidal Ni NPs with particle sizes between 3-8 nm without phosphorus-containing ligands (P-ligands).[10] They also tested the activity of Ni NPs deposited on silica support for CO_2 methanation, which resulted in high activity.[10]

This study aims to develop a procedure to synthesize size-controlled Ni nanoparticles by adapting the method reported in Vrijburg *et al.*[10] for structure sensitivity CO_2 hydrogenation catalysis. Ni NPs with different particle sizes were synthesized by changing ligands, reaction temperature and reactants ratios. These NPs were tested in catalytic activity experiments after deposition on silica support and removing the ligands. A detailed explanation of the research plan is given in the Research scope at the end of the Theoretical background.

2. Theoretical background

This chapter presents the theoretical background for using nickel-based catalysts in CO_2 hydrogenation catalysis. First, the importance of particle properties on the catalytic activity is explained, followed by the activity of Ni-based catalysts. After that, the theoretical background will focus on the colloidal synthesis of nanoparticles and ligand effects in general. Finally, the synthesis of colloidal Ni NPs and the research scope of this study is reported.

2.1. Particle size effects

Catalysts can be divided into two types: heterogeneous and homogenous. The reactants in homogeneous catalysis are in the same phase as the catalysts. In heterogeneous catalysis, the reactants are in a different phase from the catalyst. Heterogeneous catalysis will be the topic of this study, where the reaction takes place on the surface of the catalyst's active part between the catalyst (solid) and gaseous/liquid reactants. The catalyst consists of an active and a non-active part in the form of supported metal particles. The metal particles form the active part on the support and the support material forms the non-active part of the catalyst. The catalyst performance depends highly on their particle surface.

The particle size and shape can change the surface of the catalyst's active part. Since the focus of this study is the particle size effects, the effects of the shape on the activity are left out. The general idea is that smaller particles will have higher activity per gram of metal because of the higher total surface area. Because of this, more reactants could react on the surface through the high surface area. However, the particle size decrease will also change the coordination environment and electronic state of the surface atoms. The particle size decrease makes it possible that the atoms on the edges become dominant in the catalysis. For instance, Tao *et al*. prepared 2.2 nm Pt NPs where the under-coordinated Pt atoms of Pt(577) with coordination number 7 at the edges were active in CO oxidation catalysis. On the other hand, Pt atoms with coordination number 9 on the terrace of Pt(111) nanoparticles were not active.[25] In addition, metal nanoparticles smaller than 2.0 nm could behave as a molecule due to their band structure, as stated by van Bokhoven *et al*.[26] The electron density of smaller Au NPs (1.0 nm) has been shown to be greater than that of larger Au NPs (3.0 nm), revealing a clear dependence on size.[26]

However, decreasing the particle size does not always mean higher activity, as explained above. For example, the TiO_2-supported Au NPs smaller than 3.0 nm showed lower activity in CO oxidation catalysis. But also, Au NPs larger than 3 nm were less active in CO oxidation catalysis. This change in activity versus particle size resulted in a characteristic and optimum activity for supported Au NPs around 3 nm, which also applies to Ni NPs. The activity of Ni NPs will be discussed in section 2.2.

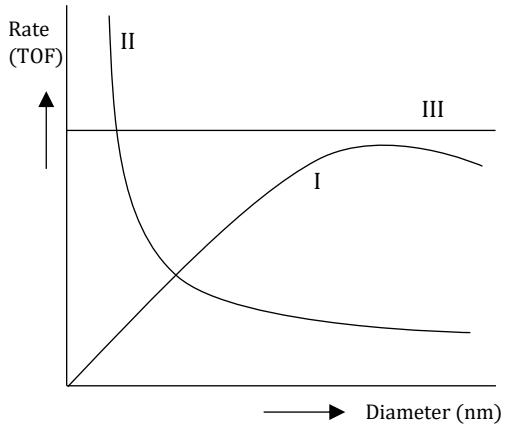

Figure 1 Three types of structure sensitivity reactions, adapted from ref. 28.

That the atoms do not have the same catalytic activity on support is called structure sensitivity, which is divided into three types (Figure 1).[21,27] Type I includes the reactions with the rate-determining step with π-bond formation and breakage. The reactions are particle size dependent with a critical size where π- bond activation is preferred on the edges. To form these edges, a minimum of atoms is necessary. This results in a

critical particle size for a maximum number of edges. Type II shows the reactions where the catalytic activity increases when the particle size decreases, and the activity decreases when the particle size increases. Finally, the particle size-independent reactions are included in type III of structure sensitivity. CO_2 hydrogenation reactions over silica-supported nickel-based catalysts show type I of structure sensitivity reactions.[2] However, the type of structure sensitivity of nickel-based catalysts could differ when the support is changed due to the support-particle interaction and porosity. For instance, recently, Visser *et al.*[28] reported that increasing the Ni nanoparticle size from 4 to 8 nm resulted in a higher catalytic activity when the Ni NPs are supported by graphitic carbon. They also showed that larger Ni NPs were most selective to methane. These all mean that controlling the Ni nanoparticle size is crucial for the CO_2 hydrogenation activity, which is discussed in the following section.

2.2.Catalytic activity of nickel-based catalysts

As hinted in the introduction, Paul Sabatier performed the first catalysis of CO_2 with hydrogen over nickel-based catalysts,[20] according to the general reaction equation 4.

$$CO_2 + 4H_2 \leftrightarrow CH_4 + 4H_2O \qquad (4)$$

In the classic mechanism,[20,29] CO_2 adsorbs with H_2 to form CO and H_2O. After that, CO can further dissociate to C_{ads} and hydrogenate to form CH_4. However, previous studies in our group have revealed that the mechanism of the Sabatier reaction could differ from the classic one.[1,2,21] Figure 2a shows the different mechanisms. CO_2 hydrogenation can follow carboxylic and formate

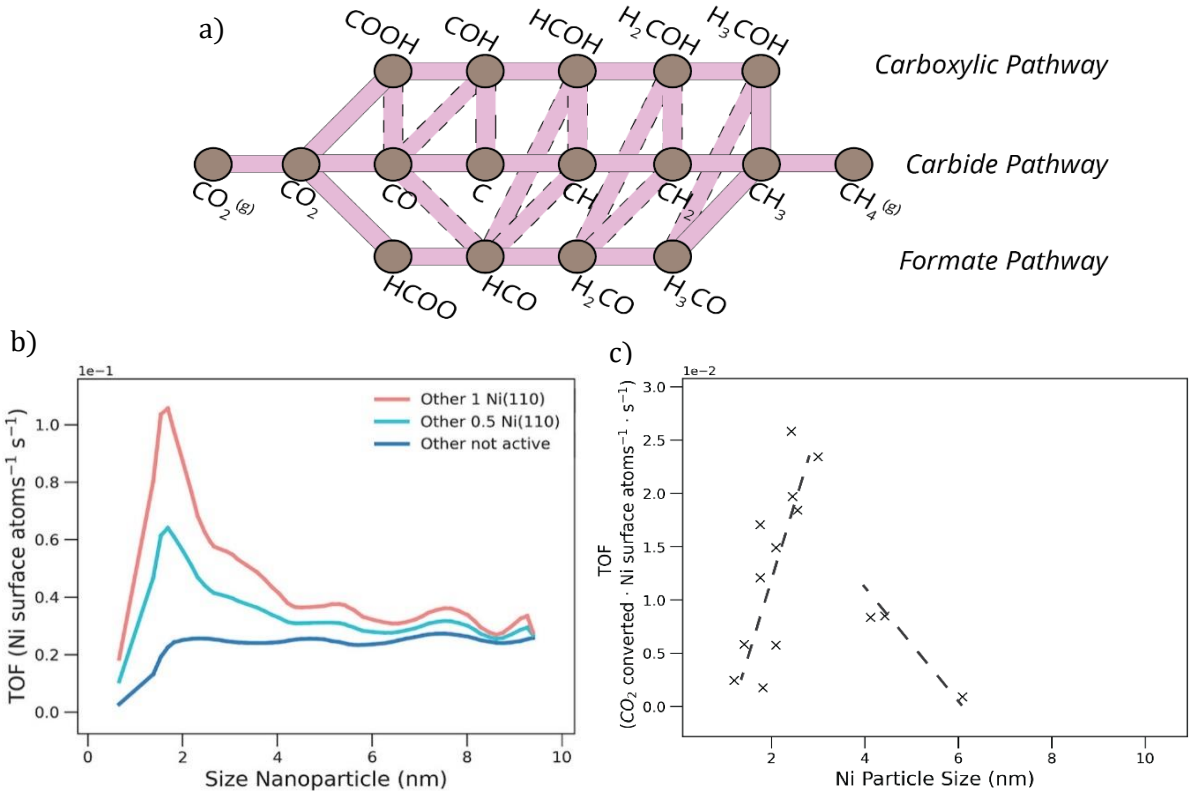

Figure 2 a) Three different mechanisms of CO_2 hydrogenation over nickel-based catalysts: carboxylic pathway (H-assisted dissociation), carbide pathway (direct CO dissociated) and formate pathway (H-assisted dissociation). The pathways are given with straight pink lines. The reactants, reaction intermediates and products are given with brown nodes. The elementary reactions between the reaction intermediates are given with dashed pink lines. b) turn-over frequency (TOF) values plotted as a function of Ni nanoparticle size, calculated with DFT and MKM . The red (1 time) and cyan (0.5 times) curves give the activity of the most active facet Ni(110), with a maximum activity around 2.5 nm particle size. The blue curves gives the activity of undercoordinated atoms, c) published experimental TOF data from Vogt et al. The figures were reproduced from Sterk et al.[2]

pathways besides the classic mechanism (carbide pathway). Carboxylic and formate pathways differ from the carbide pathway with hydrogen-assisted CO dissociation.

Sterk *et al.* showed with density functional theory (DFT) and micro-kinetics modelling (MKM) calculations that CO_2 hydrogenation over supported nickel-based catalysts follows mainly a combination of carbide and formate pathways depending on the facets. The support was not counted as an active site in the CO_2 hydrogenation catalysis. Thus the calculations are more realistic for inactive supports such as silica. The calculations were performed for four different Ni facets. It was concluded that the stepped facet Ni(110) is the most active facet during the reaction. The calculated activity plot is given in Figure 2b.[2] Next, Figure 2c shows the published experimental data from Vogt *et al.*[1] These two plots show that CO_2 hydrogenation over supported Ni catalysts follows type I of structure sensitivity. (Figure 1, Type I). The critical particle size, where the activity is at the maximum rate, is around 2.5 nm for supported Ni catalysts.

In addition, Vogt *et al.* and other works from the literature studied and discussed the formed intermediates during CO_2 hydrogenation catalysis using FT-IR spectroscopy (Figure 3).[21,30–32] FT-IR spectroscopy in operando setup makes it possible to follow the changes in IR bands of reactants, reaction intermediates and products during the catalysis experiments. According to the literature, methane peak appears at 3015 cm^{-1}, gaseous CO band appears between 2100 and 2179 cm^{-1}, on a single Ni atom adsorbed CO band appears between 2030 and 2060 cm^{-1} and bridged carbonyl CO band appears at 1918 cm^{-1}. The IR band at 1591 cm^{-1} is attributed to the formate species HCO_2^{2-} (s).[21]

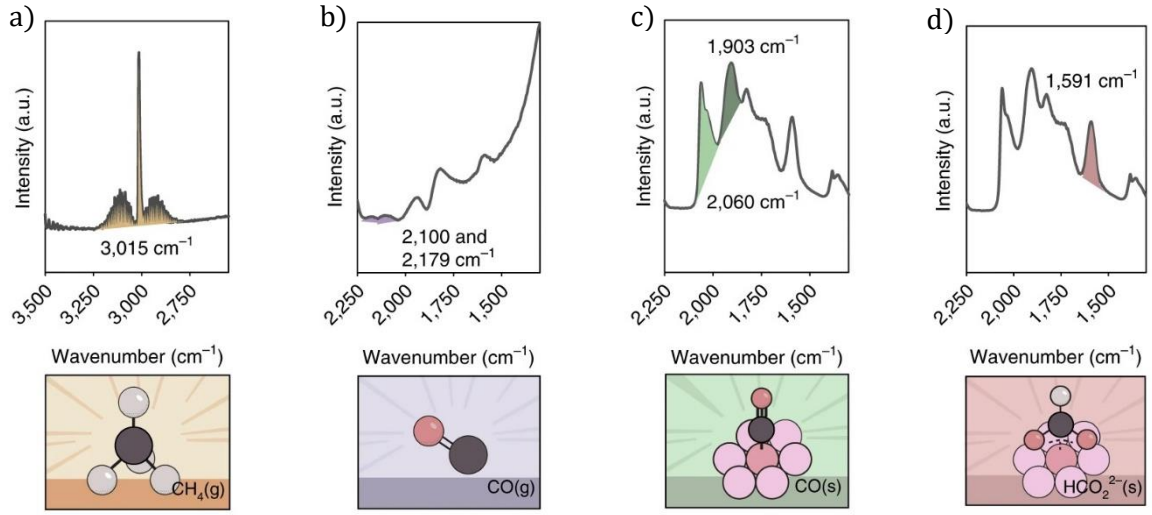

Figure 3 Assigned IR bands of the methane and intermediates during the CO_2 hydrogenation catalysis; a) methane band at 3015 cm^{-1}, b) gaseous CO band between 2100 and 2179 cm^{-1}, c) CO_{ads} (top) band between 2030 - 2060 cm^{-1} and CO_{ads}(bridged) band at 1918 cm^{-1} and d) formate species HCO_2^{2-} (s) band at 1591 cm^{-1}, duplicated from Vogt et al.[21]

2.3.Colloidal synthesis

Co-precipitation is one of the most commonly used methods, such as impregnation (deposition of metal or metal oxides onto the support) and physical and chemical vapor deposition (using evaporation) methods, for preparing heterogeneous catalysts in the literature. Vogt *et al.*[21] prepared the nickel catalysts by homogenous deposition precipitation (HDP) method, where the Ni precursor was dissolved in water with silica support while the pH was increased with an alkaline solution. The supported Ni catalyst will be prepared via a colloidal approach in this study. The colloidal method offers high control over particle size and Ni weight loading. Additionally, the

deposition of the NPs can be performed separately on different supports, allowing for simultaneous study of the effect of different supports on the catalytic activity with identical (size and shape) NPs.

A general colloidal synthesis is a heating-up synthesis in which reactants are mixed in a bottom flask, and the reaction is carried out at a specific temperature. Metal precursor, ligand, and reducing agent are the reactants. Different starting materials (metal-organic frameworks, metal complexes and open frameworks) can be used as metal precursors.[33] Among them, metal complexes are seen as the most advantageous precursor for colloidal synthesis because they are suitable for different routes of nanoparticle synthesis.[33] To prevent aggregation, a ligand and a solvent are present in the solution. They play a crucial role in controlling particle size and dispersion, as will be further explored in section 2.3.2. Next, a reducing agent is introduced to reduce the metal ion from its highest oxidation state to metallic nanoparticles. The method by which these reactants are mixed may differ, influencing the synthesis results. The two most common methods are heat-up and hot injection methods, discussed further below.[33,34]

The reactants are dissolved in the solvent in one flask in the heat-up method. The solution is then heated to the desired reaction temperature. The maximum reaction temperature is dependent on the solvent's boiling point. Heating the solution will increase the collision rate of the monomers. Then, the nucleation and growth of the particles take place when the desired reaction temperature reached.[33]

In the second method, hot injection, the agents are dissolved in the solvent in one flask (Figure 4). The metal precursor is added to another flask and dissolved in the same solvent. Both flasks are heated to the reaction temperature. The metal precursor is injected immediately at the reaction temperature to start the nucleation. There are a number of studies performed selecting different temperatures for each injection and agent's solution. Different temperatures between injection and reaction solution could also affect the particle size.[33,35]

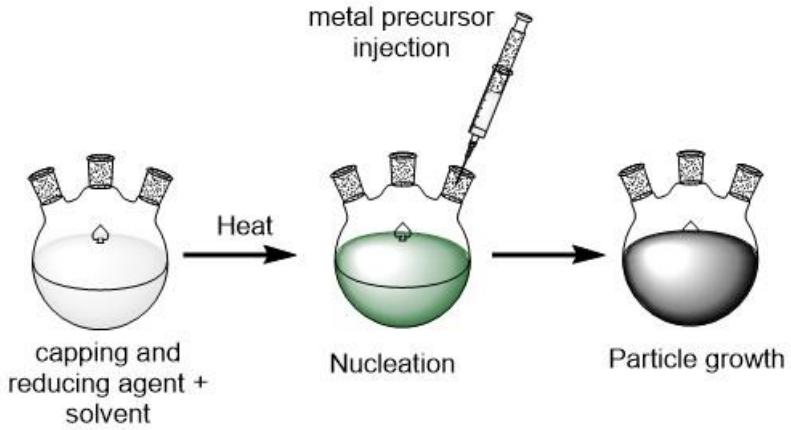

Figure 4 Representation of a colloidal synthesis with hot injection method.

In both methods, monodisperse NPs can be successfully synthesized. Although, the hot injection method is preferred when it comes to better control over the particle size and distribution. The hot injection allows a better separation of the nucleation stage from the growth stage because of the short reduction time of the metal ion. Therefore, the number of nuclei would be higher due to the reducing agent's fast reaching of the metal ion. A large amount of nuclei results in small particles with narrow size distribution. In the following section, the nucleation and growth theory will be discussed to understand the formation of nanoparticles.

2.3.1. Nucleation and growth

The classical nucleation theory is described for the first time by Gibbs. In his theory from 1876, he discussed the Gibbs free energy for the nucleation process of spherical particles.[36] It is explained by the sum of two energy terms: volume-free energy and surface-free energy. The overall growth according to Gibbs free energy is given with equations 1-3.[37,38]

$$\Delta G = \frac{4}{3}\pi r^3 G_v + 4\pi r^2 \sigma \quad (1)$$

$$\Delta G_v = \frac{-k_B T \ln(S)}{v} \quad (2)$$

$$r^* = -\frac{2\sigma}{G_v} \quad (3)$$

The first equation gives Gibbs free energy for a spherical particle. G_v is the volume free energy, σ is the surface free energy, and r is the radios of the particle. Equation 2 shows that G_v is dependent on temperature (T), the molar volume of the solid (v) and supersaturation (S). The third equation shows that the r* (critical radius) is dependent on the surface and volume energy. Herein, the critical radius forms the threshold for forming stable nuclei. All nuclei with sizes below this critical radius are prone to dissociation because of the instability. The surface free energy is greater than the volume free energy when the nucleus size is smaller than the critical radius. Upon surpassing the critical radius, ΔG decreases, and the volume free energy reaches the energy of forming a new surface. The energy required to surpass the critical radius represents the nucleation barrier for the growth of the particles.[37,38] The processes of colloidal synthesis with nucleation and growth theory are shown in Figure 5.

According to the theory, any change in temperature or molar volume of a solid will result in changes in G_v (Eq. 2), which will lead to different critical radii (Eq. 3). At constant molar volume,

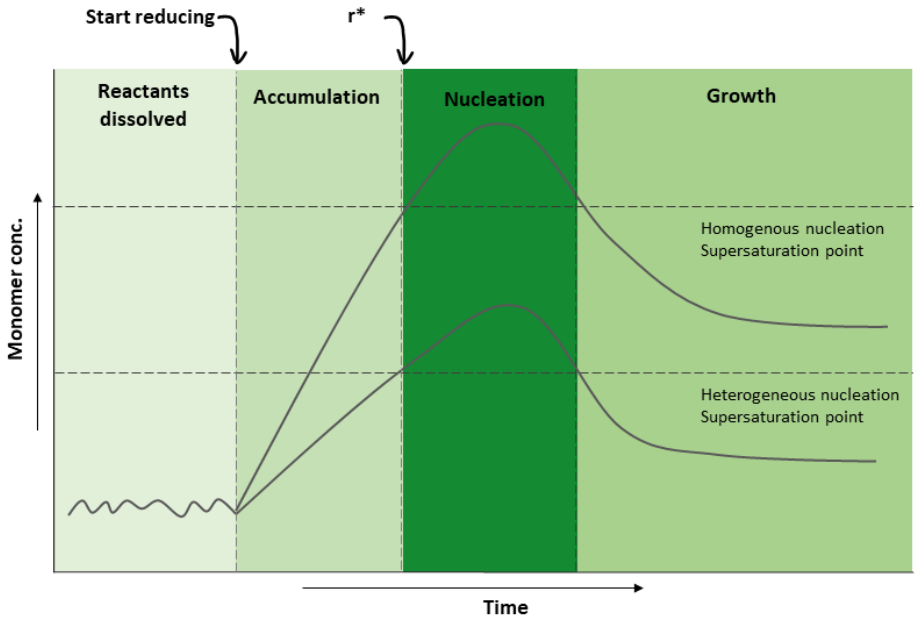

Figure 5 The steps during a colloidal synthesis with focus on nucleation and growth of the particles. Monomer concentration is plotted versus time, during the colloidal synthesis. The monomer concentration is the lowest in the first part (reactants dissolved) and increases with start of reducing. The increasing monomer concentration results in the formation of small clusters/nuclei. The formed nuclei are stable when they reach the critical radius (r), according to nucleation theory. The nucleation step starts when r* is surpassed and ends when the monomer concentration drops below supersaturation point, marking the start of particle growth. Two curves correspond to two nucleation methods: homogeneous and heterogeneous nucleation. The figure was reproduced from ref. 38.*

a higher temperature will lead to a smaller critical radius. On the other hand, the higher molar volume will lead to a larger critical radius at a constant temperature. Additionally, supersaturation is responsible for reaching the intense collision of the monomers. Intense collision is responsible for the nucleation duration, which is the supersaturation point in the literature.[39] The nucleation step takes place quickly and will stop after dropping the supersaturation level below the level at the beginning of the nucleation step. After stopping the new nuclei formation, existing nuclei can grow by consuming other monomers. The growth of the particles is entirely dependent on the number of nuclei. This growth step will continue until the solution is no more supersaturated. More nuclei will result in small particles, and few nuclei will result in larger particles.[37,38]

The nucleation step could follow two different ways: homogenous and heterogeneous nucleation (Figure 5 and Figure 6). Homogeneous nucleation is the path whereby the atoms form the nuclei from the beginning. On the other hand, the monomers are added to a nuclei-containing (seeds) solution called heterogeneous nucleation. The nucleation barrier applies to both nucleation processes, but the nucleation barrier is lower in heterogeneous nucleation. The heterogeneous nucleation barrier is half of the homogenous nucleation barrier when a particle is assumed in a spherical shape (Figure 6).[37,38] Therefore, the heterogenous nucleation is important and advantageous when lower energy use is desired. However, heterogeneous nucleation will be avoided in this study since exploring the effect of changes on homogenous nucleation is the goal of this study. Hence, the discussion will be further based on homogenous nucleation.

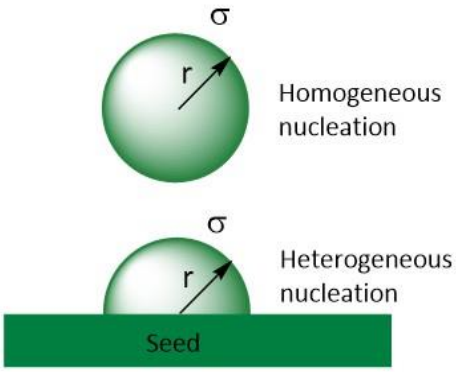

Figure 6 Homogeneous and heterogeneous nucleation, adapted from ref. 37.

The particle growth and size distribution are dependent on the nucleation barrier. Without a nucleation barrier, the growth would follow a growth like polymerization resulting in polydisperse particles. During the polymerization, polymers start forming from one monomer, without a barrier, to very long-chain compounds. Because of this barrier, the monomers are kept "ready" to form nuclei until they reach the critical point. To achieve a narrow size distribution (monodisperse), nucleation should occur quickly and be separated from the growth stage. Polydisperse particles will result if the growth step begins while nucleation is not completed. This process is known as ongoing homogeneous nucleation. Rapid reduction of metal precursors is proposed using various reducing agents to prevent the ongoing homogenous nucleation. Therefore, the hot injection method is one of the most used rapid reduction methods. For instance, Yin *et al*. explained that rapidly injecting metal precursors will make separating nucleation and growth possible. By rapid injection, nucleation induces after immediately dropping the saturation level.[40] Further, ΔG of the spherical particles is also affected by the presence of ligands, stabilizing the nanoparticles in the solution. This effect of the ligands is covered in the next section.

2.3.2. Ligand effects

In the colloidal approach, the inorganic core is surrounded by an organic (ligand) shell formed from polar and non-polar heads to stabilize the NPs. The role of the ligand is crucial for the forming of NPs. Ligands stabilize the NPs by electrostatic repulsion, steric effects and a combination of both. For example, highly charged ligands use their electrostatic repulsion property, while other ligands use steric effects thanks to their geometrical properties, see Figure 7.[41]

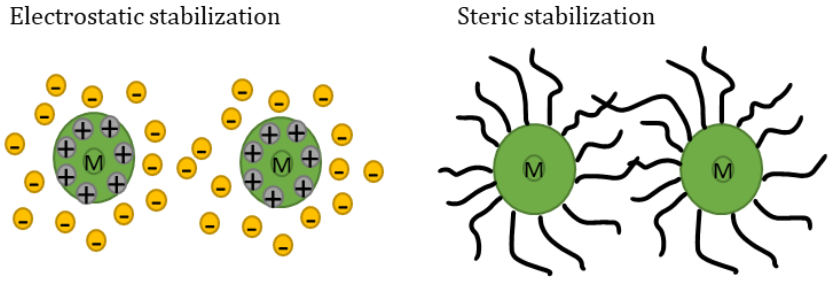

Figure 7 Electrostatic and steric stabilization of NPs by ligands.

Apart from the thermodynamics and kinetics of growth, ligand-NP interaction has a thermodynamic driving force which is responsible for the crucial role in determining the particle size and shape.[38] Thermodynamically, the most favourable particle size or shape has the minimum total free energy (ΔG). The attachment of ligands to the surface of NPs reduces the surface energy of the NPs by adsorbing them onto their surface. This minimizes the effect of surface energy (σ) during nuclei formation.[38]

On the other hand, kinetically, the ligand could affect the NPs size through how these ligands are capped at NPs. The ligand forms a barrier for the deposition of monomers on NPs. Adsorption of the ligands on NPs is a dynamic process. They constantly adsorb and desorb on the NPs during the growth step of the particles by forming and breaking bonds. Therefore, metal monomers must wait to participate in the growth stage until a ligand is desorbed from the NPs. Here, the geometrical structure of the ligand with functional groups, the ligand-metal interaction, ligand-solvent interaction and ligand-ligand interaction could affect the particle shape and size.[38,42]

Larger (bulkier) ligands result in larger NPs because they slow down the formation of new nuclei. The existing nuclei can grow further by consuming other monomers because the surface energy is minimized. The desorption of the ligand could be difficult if the ligand-ligand interactions are very crowded and packed.[43] In general, the literature shows that ligands with strong interaction (e.g., thiolates[44]) with NPs give strong stability and high size control availability to the NPs. Weak ligands (amines, alcohols) give less stability to the NPs.[45] However, strong ligands decrease the catalytic activity strongly, while weak ligands give higher activity.[46] As an example of strong ligands, Yoskamtorn *et al.* covered supported Au_{25} clusters with thiolates as ligands to use them in benzaldehyde formation. They observed that the benzaldehyde selectivity was improved when the thiolate amount on the Au_{25} cluster was increased while the activity was reduced.[44] On the other hand, Moreno *et al.* have compared the activity of octylamine-coated Pd MPCs (3.0 ± 0.8 nm) with hexanethiolate-coated Pd MPCs (3.0 nm). They reported that octylamine-coated Pd MPCs were more active but unstable when compared to hexanethiolate-coated Pd MPCs.[45] In the next section, the colloidal synthesis of Ni NPs in the literature and the aim and method of this study will be explained, focussing on the changes during the synthesis.

2.4.Synthesis of colloidal Ni NPs

Synthesis of colloidal Ni NPs is mainly performed by thermal decomposition and the external reducing agent method. The often-performed method is the thermal decomposition method, where the ligand is used as the reducing agent.

In the literature, $Ni(acac)_2$ is mainly used as a Ni precursor and oleylamine (OAm) is used as a ligand.[10,18,47] Thermal decomposition with $Ni(acac)_2$ and OAm resulted in polydisperse 22 nm Ni NPs in Zhang *et al.*,[47] and in 10-50 nm NPs when alkylamines were used as the reducing agent in Chen *et al.*[18] This wide size distribution was resolved using stronger ligands, such as phosphorous-containing (P-ligands). For instance, Carenco *et al.* synthesized monodisperse Ni NPs with particle sizes between 2-30 nm using a combination of trictylphosphine (TOP) and OAm.[48] Despite, P-ligands resulting in monodisperse Ni particles, they also incorporate into the Ni lattice. Because of this incorporation into the Ni lattice, their removal becomes insufficient, which makes the catalyst inactive.[22] Therefore, using P-ligands is avoided in this study.

Instead of using P-ligands, stronger reducing agents were added to control the particle size. Borane tert-butylamine (BTB) complex is accepted as a promising reducing agent for colloidal Ni NP synthesis. One example important for our study is the work of Metin and co-workers.[24] They could synthesize monodisperse Ni NPs with particle size between 3.2 and 5.4 nm by injecting (hot) BTB as a reducing agent, where $Ni(acac)_2$ was the metal precursor, and OAm and oleic acid were the ligands and solvents. The particle size was controlled by changing the BTB/Ni ratio.

After that, Vrijburg *et al.*[10] synthesized colloidal Ni NPs by adapting the method of Metin *et al.*[24] which will form the basis for our synthesis method. $Ni(acac)_2$, OAm and oleic acid were added to a round-bottomed flask. Then, BTB dissolved in OAm was injected at 90 °C into the solution as the reducing agent. Yielded Ni NPs were between 3 and 4 nm particle size and were used as seeds. To synthesize larger particles, heterogenous nucleation was performed on obtained seeds. The solution of seeds was heated to 220 °C, and additional Ni precursor and ligand were added dropwise to the solution, which yielded 5-8 nm Ni NPs.

2.4.1. Research scope

This study aims to synthesize colloidal Ni NPs with particle sizes between 1-7 nm for structure sensitivity CO_2 hydrogenation catalysis. We adapted the colloidal Ni NPs synthesis method (Scheme 1), reported by Vrijburg *et al.*[10] and Metin *et al.*[24]

Three parameters will be changed to control the particle size and particle size distribution: 1) reaction temperature, 2) ligands, and 3) reactant ratios. An overview is given in (Scheme 1) for the colloidal synthesis of Ni NPs with benzonitrile as a ligand. Benzonitrile, 2,4,6-trimethylaniline (mesitylamine) and 4-tert-butylbenzonitrile will be used as ligands during the synthesis instead of OAm. The synthesis solvent will be toluene instead of OAm or oleic acid. Toluene can be removed in the vacuum due to its low boiling point and high volatility. The motivation for selecting these ligands was the proven interaction with Ni NPs of N-containing ligands, such as the interaction of OAm with Ni NPs[47] and their small sizes compared to the OAm ligand. As explained in the Ligands effects section, these small ligands will result in smaller NPs. Besides, these ligands will be soluble in toluene which supports the choice of the ligands.

According to the nucleation and growth theory, decreasing the temperature will increase the particle size. Therefore, the reaction temperature will be lowered from 90 °C to room temperature. The effect of the reactants will be studied by changing the ratios of the reactants between 1/5. Besides the change in the particle size, it will be focused on the particle size distribution. By applying these changes, five catalysts with different particle sizes will be prepared by depositing Ni NPs on silica (Scheme 1, **4** to **5)** and removing the ligands (Scheme 1, **5** to **6**).

Another objective of this study is the chemical removal of the ligands from the Ni NPs. In the literature, the ligands were mainly removed by calcining the supported Ni NPs at high temperatures.[22] It turned out that calcination at high temperatures led to the sintering of Ni NPs, which is not preferred in structure sensitivity reactions because of particle size effects. Therefore, to avoid sintering, the ligands will be removed by alkylating the ligands using Meerwein's reagent. Rosen *et al.*[49] and Nelson *et al.*[50] reported a successful ligand removal using Meerwein's reagent. PbSe films of Rosen *et al.* were prepared with oleate ligands. These ligands were stripped using Meerwein's reagent, resulting in conductive PbSe films, while the films were not conductive before Meerwein's treatment. Also, Nelson *et al.* found clean surfaces when Meerwein's reagent alkylation was applied. In the last part, we will test our catalysts in structure sensitivity CO_2 hydrogenation catalysis to relate the catalytic activity with particle size.

In summary, the following goals are targeted in this study: 1) synthesizing of colloidal Ni NPs between 1 and 7 nm particle size by changing the reaction temperature, ligands, and reactant ratios, 2) the deposition of synthesized colloidal Ni NPs on the silica support, 3) removing the ligands from supported Ni NPs by applying a chemical treatment method using Meerwein's reagent and 4) testing the catalytic activity of silica-supported colloidal Ni NPs in the CO_2 hydrogenation reactions and relating the activity to particle sizes. The characterization will be done using TPR, TEM, AAS, and operando FT-IR spectroscopy. The methods and materials will be given in the next chapter, Experimental methods.

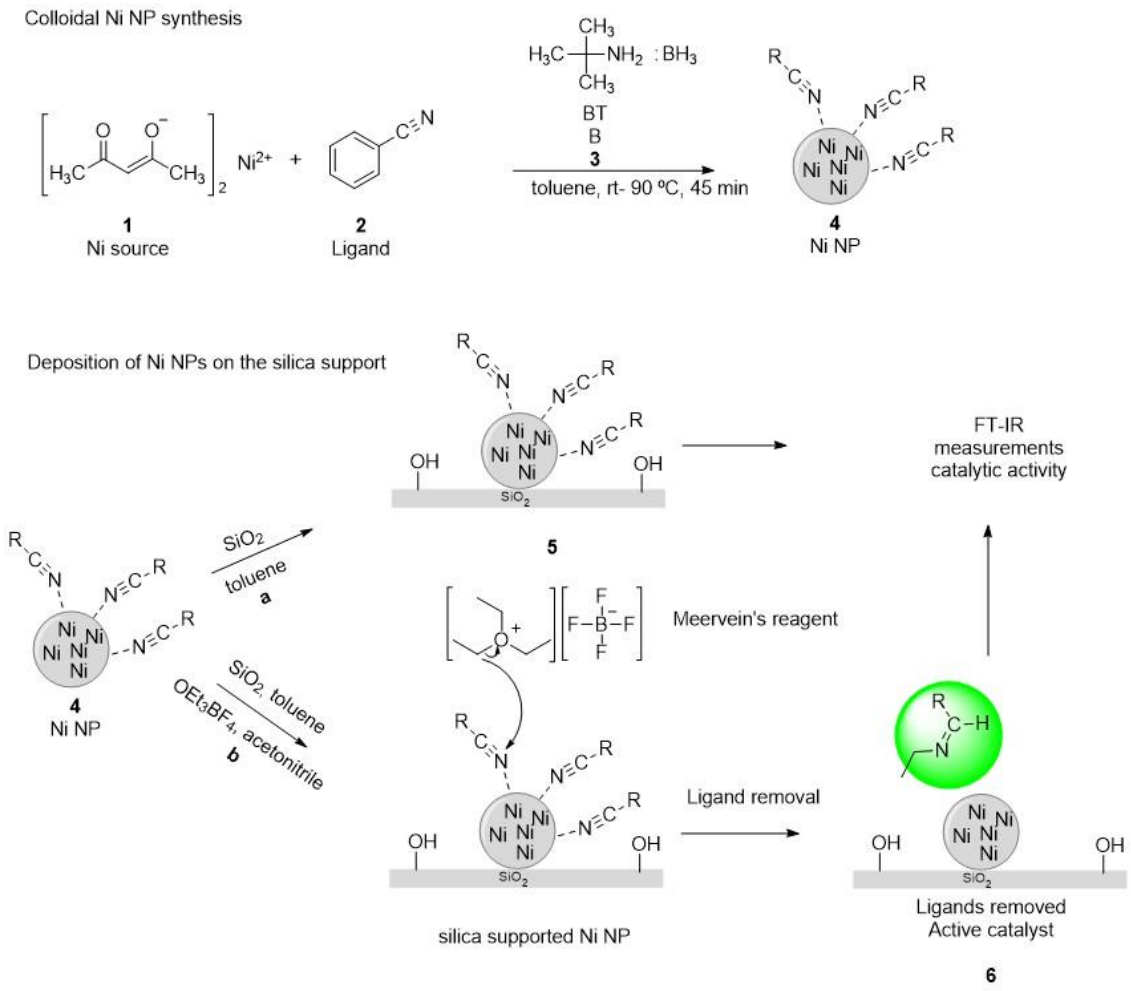

Scheme 1 Preparation overview of the silica supported colloidal Ni NP catalysts in this study.

3. Experimental methods

3.1. Materials

All chemicals used during the experiments were purchased from Sigma-Aldrich unless otherwise stated. All used solvents were degassed by purging with N_2 for at least an hour and dried over molecular sieves. Nickel(II) acetylacetonate(95%) was used as the metal precursor for the synthesis of Ni NPs. Manganese(II)acetylacetonate, iron(III)acetylacetonate(97%), cobalt(II) acetylacetonate(97%), copper(II) acetylacetonate(97%) and ruthenium(III) acetylacetonate(97%) were chosen as metal precursors for the syntheses of other metal NPs. The ligands were benzonitrile (99%), 2,4,6-trimethylaniline (98%), and 4-tert-butylbenzonitrile. 4-tert-butylbenzonitrile (98%) was purchased from Fisher Scientific. Borane tert-butylamine (BTB) complex (97%) was the only reducing agent during the syntheses. Toluene was the reaction solvent. Hexane and tetrahydrofuran (THF) were used for washing the products.

3.2. Synthesis of colloidal nickel nanoparticles

The synthesis was carried out in an inert environment using an atmosphere of nitrogen. First in the glove box, 257 mg (1 mmol) $Ni(acac)_2$ (metal precursor), 0.309 ml (3 mmol) benzonitrile (ligand) and 15 ml toluene were added to the first Schlenk flask. In the second Schlenk flask, 264 mg (3 mmol) BTB (reducing agent) and 10 ml toluene were added. Then both flasks were transferred to the Schlenk line and heated up to 80 °C to dissolve the starting material completely. After dissolving at 80 °C, both flasks were heated to the desired temperature: 90 °C. If the desired temperature was lower than 80 °C, they were cooled down while stirring after dissolving at 80 °C. Usually, the BTB solution was injected quickly at 90 °C. The color of the solution was changed from green to black within 30 s. Toluene was evaporated after 45 minutes of stirring at 90 °C and the Schlenk flask was transferred to the glove box. The product was washed with hexane (3 times) with one-time sonification (3 min) and three times centrifugation (5 minutes, 3000 RPM) and dried in the vacuum. This yielded a dark brown-black powder.

3.3. Deposition of Ni NPs on the silica support, treated with Meerwein's reagent

It was assumed that 100% Ni (59 mg Ni) was yielded from the synthesis. Therefore, the dark-brown Ni NP powder was dissolved in 10 ml toluene in the glove box to get a solution of approximately 6 mg/ml Ni. However, the actual Ni weight loading would be lower. To another vial, 1500 mg SiO_2 and 15 ml toluene were added. Then, 6.24 ml of Ni/toluene (6.24 ml=37.4 mg Ni) was added to the vial with SiO_2 to get 2.5 wt.% (37.4 mg/1500 mg silica). The solution was stirred for at least 30 minutes. In another vial, 207 mg of Meerwein's reagent was weighted with 5 ml acetonitrile as solvent. After stirring for 30 minutes, Meerwein's reagent with acetonitrile was added carefully to the vial with silica and Ni NPs and left again for stirring for 1 hour. The solvents were then removed after centrifuge (5 min, 3000 RPM). The product was washed (THF) and centrifuged (5 min, 3000 RPM) twice. The product was dried in the vacuum in the glove box. A light brown silica powder was obtained.

Sample labelling

In this report, the name of the samples is given first with the abbreviation of metal nanoparticle, then by the ligands in brackets, followed by the particle size. If the product was further adapted by supporting or ligand removal treatment, then a @ is added to the name, followed by support material and ligand removal reagent. If a ligand removal was performed, then the ligand in brackets is omitted. For example, silica-supported 4.0 nm Ni nanoparticles with benzonitrile as the ligand and treated with Meerwein's reagent to remove the ligands are given as

NiNP4.0@SiO_2Mw. The ligand in the bracket is removed because Meerwein's reagent removes the ligand from the NPs. Otherwise, it will be NiNP(PhCN)4.0@SiO_2 without Meerwein's reagent. The following chapters cover the materials and methods for preparing active Ni catalysts.

3.4.Characterization techniques

Transmission Electron Microscopy (TEM)
The TEM images were acquired with an FEI Technai 20 Transmission Electron Microscopy. It was operated at a voltage of 200 kV with a tungsten filament. The TEM samples after the colloidal synthesis were prepared by dispersing them with toluene. The preparation of the TEM samples after IR measurements were done by diluting them in ethanol. TEM images were analyzed using ImageJ software by measuring the diameter of the particles. Unless otherwise stated, all of the TEM images are made by the author.

Temperature Programmed Reduction (TPR)
The reduction temperatures were measured using Altamira Instruments (AMI-300IP). Samples of around 50 mg were used in a U-tube. First, the sample was dried at 120 °C for 30 min. Then it was heated with an increase of 5 °C/min to 800 °C in 5% H_2 in Ar, while the reduction temperature was determined by measuring the gas consumption using the Thermal Conductivity Detector (TCD).

Atomic Absorption Spectroscopy (AAS)
AAS measurements were done using contrAA® 700 High Resolution Continuum Source Atomic Absorption Spectrometer from analytikjena with acetylene flame. The calibration sequence was prepared for a range between 0-60 mg Ni in 1000 ml water. The AAS samples were prepared by diluting 30-130 mg catalysts in 25 ml or 50 ml with 2-3 ml 60 % nitric acid in a volumetric flask. The silica support was filtered using filter paper. Then the atomic absorption was measured triple for every sample, and the average value was taken. Finally, the concentration of Ni was calculated using the polynomial degree based on the calibration sequence.

Catalytic experiments using operando Fourier-Transform Infrared spectroscopy (FT-IR)
IR measurements were done using Bruker Tensor 37 and Tensor 27 FT-IR spectroscopes equipped with Mercury-Cadmium-Telluride (MCT) or Deuterated Triglycine Sulfate (DTGS) detectors. FT-IR spectroscopes were equipped with a transmission cell (High Temperature High

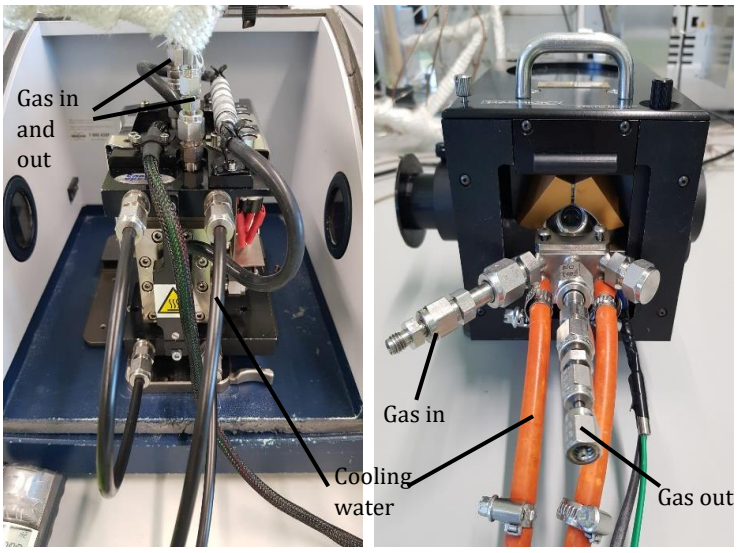

Figure 8 (Left) The transmission cell from Specac and (Right) DRIFTS cell from Harrick Scientific Products.

Pressure, HTHP) from Specac (Figure 8, left), a DRIFTS cell (The Praying Mantis™ High Temperature Reaction Chamber) from Harrick Scientific Products (Figure 8, right) and ATR-IR. When using the transmission cell, pellets were made of 15-35 mg samples. For the DRIFTS cell measurements, the samples were sieved between 75 - 212 µm, and 10-35 mg was typically used. Calcination experiments were usually performed in O_2 flow, but N_2 or air was also used. The reduction experiments were performed in H_2/N_2 flow, and the CO_2 hydrogenation experiments were carried out in H_2, N_2 and CO_2 flow. CO_2 hydrogenation was started by heating the sample from 200 °C to 400 °C with a flow of CO_2/H_2 (1/4). The CO_2 hydrogenation step was also held for one hour at 400 °C. A typical representation of the reduction and CO_2 hydrogenation experiments is given in Figure 9 with conditions.

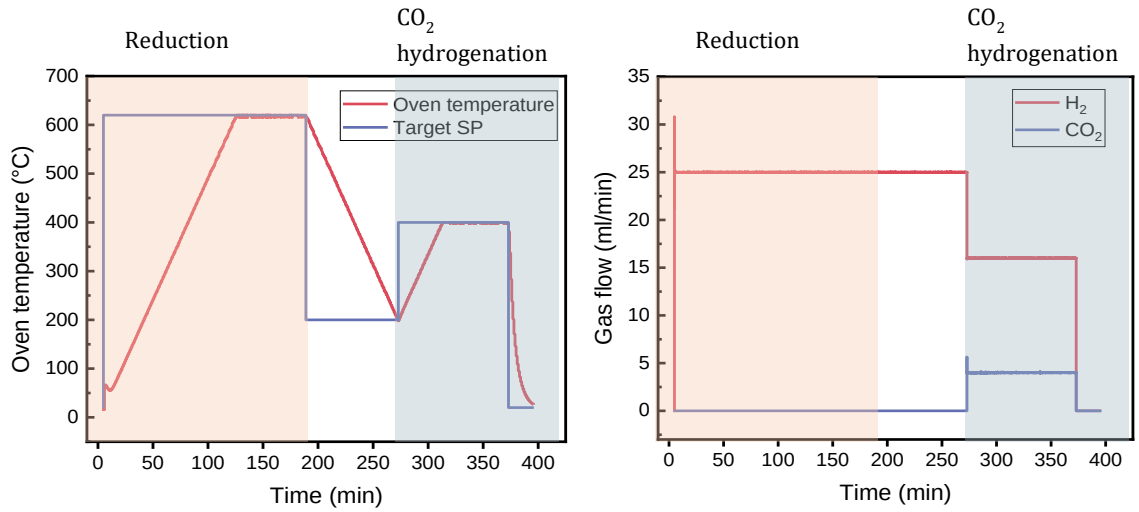

Figure 9 Representation of the reduction and CO_2 hydrogenation experiments. (Left) The temperature change versus time (min) is plotted during the reduction and CO_2 hydrogenation reactions. Red line gives the actual oven (cell) temperature, and the purple line gives the target temperature point . (Right) The gas flows of H_2 and CO_2 versus time (min) are plotted. Red line gives the gas flow of H_2 and the purple line gives the gas flow of CO_2.

4. Results and Discussion

In this chapter, every step to develop a method to synthesize size-tunable colloidal Ni nanoparticles will be discussed in separate sections regarding the changes in the synthesis. The catalytic activity of the colloidal Ni NPs during CO_2 hydrogenation will be discussed after explaining the deposition and ligand removal results.

4.1.Colloidal Ni nanoparticles synthesis

Ni nanoparticles were synthesized via the colloidal approach, whereby the nickel precursor, $Ni(acac)_2$, ligands and the solvent were heated. Then, the reducing agent (BTB) was injected quickly (hot injection) at a desired high temperature to start nucleation and particle growth. Khan *et al.* described that, in general, the metal precursor was injected into the solution of ligand and reducing agent.[33] But during our syntheses, we injected the reducing agent to the solution of Ni precursor with the ligands instead of injecting metal precursor. It was assumed that the metal monomers could be better solvated by the ligand and solvent.

The washing step was an issue after terminating the synthesis and removal of toluene in the vacuum. Different organic solvents (isopropyl alcohol, acetone, pentane) were used to wash the product after cooling down. They were oxidizing the Ni NPs in the solution, which was observed in the color change from black to a colorless solution. The oxidation of Ni NPs made it challenging to follow the washing step because the phase boundaries were unclear. Dried hexane was found as a working solvent to wash the product. Initially, the product was washed three times quickly inside the glove box without waiting. The washing resulted in TEM images with large needle-like shapes (Figure SI 1a). It was concluded that they were organic materials (waste) from the reaction after comparing them with the TEM image of the hexane waste (Figure SI 1b). The most efficient washing procedure was determined as washing with hexane solvent three times, including sonification (5 min) and centrifugation (5 min, 3000 RPM). The TEM images with clear Ni NPs and some organic compounds were obtained, as in Figure 11.

A number of different syntheses were carried out by varying reaction temperatures, different ligands, and different ratios of reactants to synthesize Ni NPs with different nanoparticle sizes. The synthesized Ni NPs were tested for their effect on the catalytic activity in CO_2 hydrogenation catalysis. During all the syntheses, nickel acetylacetonate was used as Ni precursor, and BTB was used as the reducing agent. A summary of these syntheses is given in Supplementary Information 2 (Table SI 1) and a representation of the synthesis is shown in Figure 10.

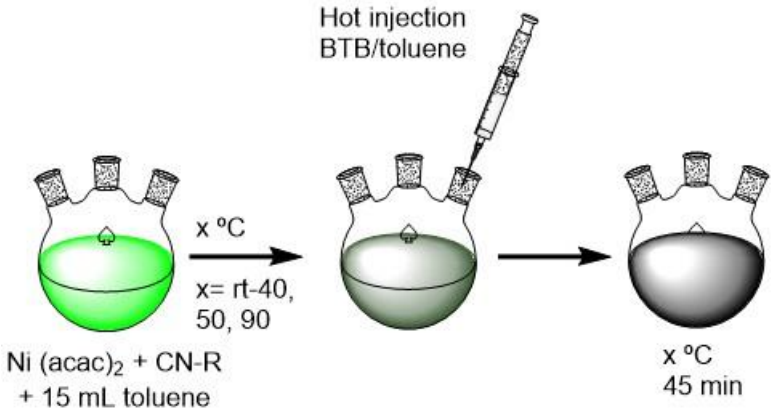

Figure 10 Illustration of the colloidal synthesis process with $Ni(acac)_2$ (metal precursor), CN-R (ligands), toluene (reaction solvent) and hot injection of BTB/ toluene into the synthesis flask at temperatures rt-40, 50 and 90 °C. The color change of the solution from green to black represents the nucleation of Ni NPs.

We discuss these syntheses under three different sections: 1) reaction temperature effect, 2) ligands effect and 3) effect of different ratios of reactants. The reaction temperature effect was studied by decreasing the temperature from 90 °C to room temperature while other parameters were held constant. The ligand effect on the Ni NPs was explored using different ligands in the syntheses, while the reaction temperature with other parameters was held constant. In the last one, the ratios of precursor, reducing agent and ligand were changed to study the effects of the changes on the Ni NP sizes.

4.1.1. Reaction temperature effects

The colloidal Ni NPs were synthesized at three different reaction temperatures (rt-40, 50 and 90 °C), and the particle sizes were determined with TEM. During these syntheses, benzonitrile was chosen as the ligand. The ratios of the reactants (Ni precursor/BTB/ligand, 1:3:3) were the same at every synthesis.

The color change from green to black (nucleation) after injecting the BTB solution was very fast, within a couple of seconds, when the synthesis was performed at 90 °C. The high temperature ensured that nucleation would occur fast. This resulted in small nanoparticles with an average size of 2.1 nm (Figure 11a) and a low 0.4 nm (17.0 %) standard deviation, which is acceptable for monodisperse particle sizes.

After synthesizing at 90 °C, the reaction temperature was set at 50 °C. The aim of choosing a quite low reaction temperature was to obtain Ni NPs with significantly different particle sizes than the Ni NPs after the synthesis at 90 °C. Synthesis at 50 °C resulted in particles with an average size of 2.8 nm and a standard deviation of 0.5 nm (20.6%) (Figure 11b). A larger standard deviation value was expected because after reducing agent injection, the nucleation of the Ni NPs at 50 °C took much longer (30 seconds) than at 90 °C.

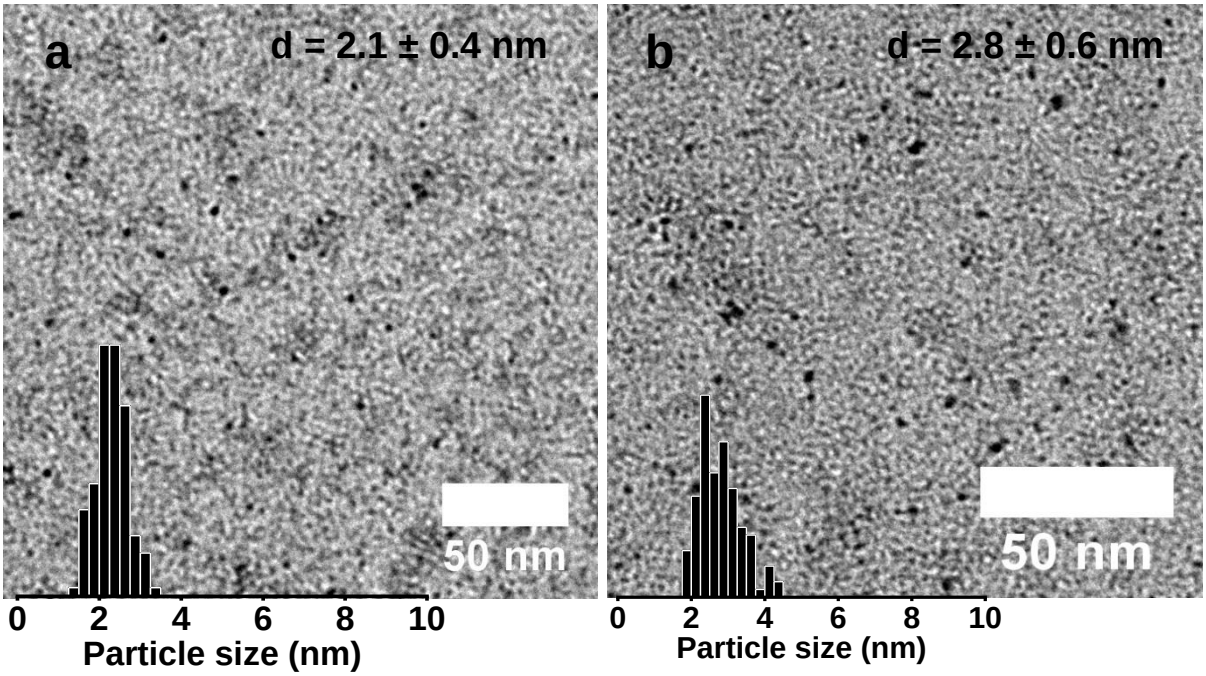

Figure 11 TEM images of colloidal Ni NPs after washing with hexane, synthesized at different reaction temperatures a) 2.3 nm Ni nanoparticles (NiNP2.3) synthesized at 90 °C, b) 2.8 nm Ni nanoparticles (NiNP2.8) synthesized at 50 °C.

The last synthesis where the Ni NPs were synthesized was started at room temperature, but the nucleation did not start right after the injection of the reducing agent at room temperature. The room temperature was not high enough to reach the saturation point because of the slow reaction rate to reach the saturation point. Therefore, the temperature increased first to 30 °C then to 40 °C. The nucleation did not occur at 30 °C, but a slight color change was observed at 40 °C, indicating the start of nucleation. Within half an hour, the color of the solutions was changed to black. Long nucleation time can be seen in the standard deviation of the particle size, 1.3 nm (29.5%), with an average particle size of 4.4 nm (Figure 12).

The results of varying the reaction temperature are in line with the expectation from the nucleation and growth theory. Lowering the reaction temperature will lead to larger nanoparticles and more polydisperse distribution in the particle sizes. Due to the low reaction temperature, the accumulation of the monomers was preferred, and the oversaturation of the solution was reached slowly. Low temperature resulted in a small value for ΔG_v, resulting in a larger critical radius. Therefore, fewer new nuclei were formed, stimulating the growth of the existing nuclei. Subsequently, nucleation took place slowly at low temperatures after hot injection because of the slow oversaturation. Slow and long nucleation was indicated by slowly changing the color from green to black. However, long nucleation showed that reactions were still ongoing and new nuclei were forming. These newly formed nuclei had less time to grow after the hot injection, and the particles from these nuclei became smaller than before the hot injection, resulting in less monodisperse Ni NPs. Less monodispersity explains the range of standard deviations (from 0.4 to 1.4 nm: 17.0 - 29.5%) of the syntheses by decreasing the reaction temperature.

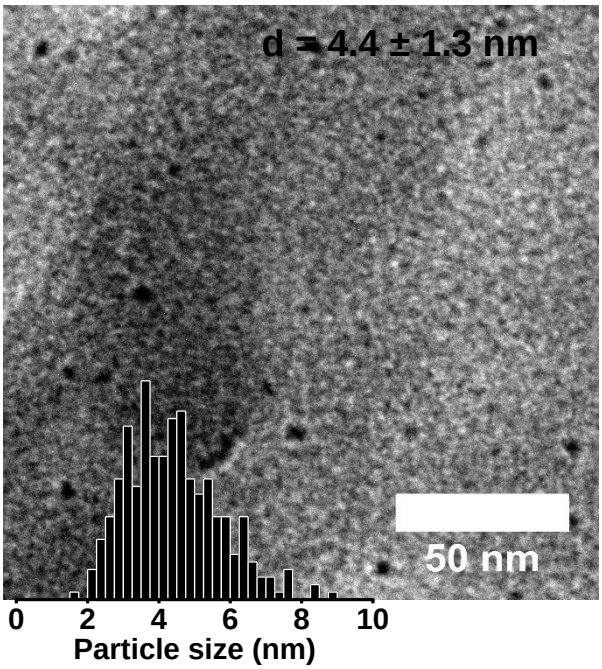

Figure 12 TEM images of 4.4 nm colloidal Ni nanoparticles (NiNP4.4) after washing with hexane, synthesized at rt-40 °C.

The particle size distribution was still acceptable compared to the literature values. Vrijburg *et al.* reported for their colloidal Ni NPs a standard deviation between 11. 4% and 19%.[10] Vogt *et al.* reported a standard deviation difference between 20% (1.8 ± 0.3 nm)[1] to 54% (4.4 ± 2.4 nm)[21] for Ni NPs after reduction experiments. It is a well-known phenomenon that Ni NPs are sintering at high temperatures.[22] Therefore, we also expect an increase in the particle sizes of our colloidal Ni NPs after the reduction at high temperatures, which will be mentioned in the discussion of catalytic activity experiments. The following section will discuss the effect of different ligands on particle size.

4.1.2. Ligands effects

The second main change in the synthesis of colloidal Ni NPs was changing the ligands. According to the literature, more bulky ligands should give larger nanoparticles. For example, Sahu *et al.* described the synthesis of CdSe nanoparticles using mercaptoacetic acid and starch as ligands. The synthesis with mercaptoacetic acid (small molecule) resulted in CdSe nanoparticles around 5 nm particle size, while the synthesis with starch yielded CdSe nanoparticles around 15 nm.[51]

Three different ligands were used during the syntheses in order to reveal the effects of the ligand: benzonitrile, 2,4,6-trimethylaniline (mesitylamine) and 4-tert-butylbenzonitrile (Figure 13). The ratios of the reactants (Ni precursor/BTB/ligand, 1:3:3) and the reaction temperature (90 °C) were the same during the syntheses. The choice for the ligands was supported by having nitrogen-containing functional groups but different sizes and geometry.

Figure 13 Molecular structures of the used solvent(toluene) and ligands.

The synthesis results with benzonitrile are given in Figure 11a. An important point to mention about the synthesis with benzonitrile is the low value of the standard deviation of 0.4 nm (17.0%) with 2.1 nm particle size. The synthesis using the mesitylamine resulted in 3.8 nm particles (Figure 14a) with a standard deviation of 0.5 nm (13.7%). Herein, the organic compounds from the initial reactants were not washed clearly. Therefore, the particles were found within the organic materials (dark background) in the TEM image. The synthesis with 4-tert-butylbenzonitrile gave Ni nanoparticles of 3.4 nm with a standard deviation of 0.9 nm (26.5%).

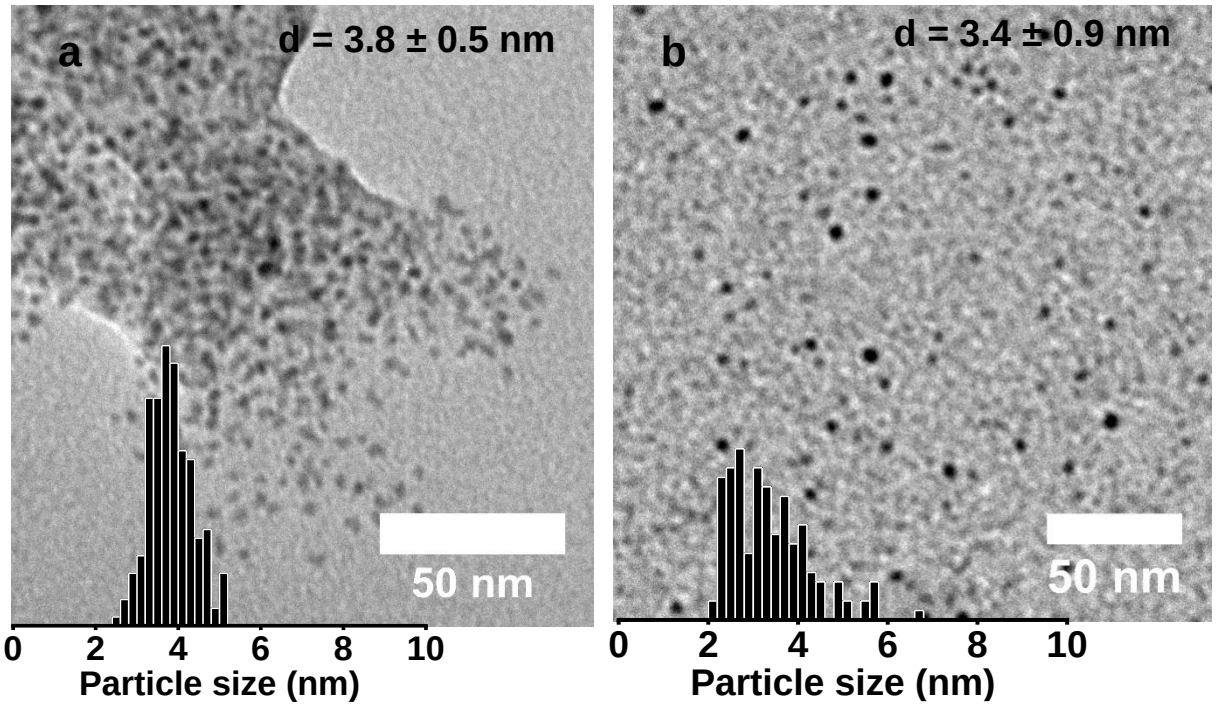

Figure 14 TEM images of colloidal Ni NPs after washing with hexane, synthesized with different ligands a) 3.8 nm Ni nanoparticles after synthesis with 2,4,6-trimethylaniline (By Bram Kappé, reprinted with permission), b) 3.4 nm Ni nanoparticles after synthesis with 4-tert-butylbenzonitrile ligand.

The results of these syntheses match the expectation. Smaller particles were expected with benzonitrile after considering the molecular size and geometry of benzonitrile and the other two ligands. Benzonitrile is a smaller compound (short chain length and no other functional groups creating steric hindrance) than the other two ligands. Benzonitrile was responsible for a larger number of nuclei in the solution during the accumulation step. More nuclei resulted in smaller NPs due to the collision of these nuclei. Additionally, benzonitrile has a very similar geometry as the synthesis solvent, toluene. Therefore, the interaction (π-π stacking) difference between the ligand and toluene solvent was minimum in this case. The saturation point was reached at a high rate using benzonitrile than the other ligands. Other ligands contain extra functional groups (methyl), which had enlarged the interaction difference between the ligand and toluene solvent due to the steric hindrance.

On the other hand, mesitylamine and 4-tert-butylbenzonitrile are larger molecules than benzonitrile. Therefore, they resulted in larger Ni NPs than the Ni NPs after synthesis with benzonitrile as the ligand. The geometry of mesitylamine and 4-tert-butylbenzonitrile reveals that using mesitylamine as a ligand will create fewer nuclei because the methyl groups are on every side of the molecule. The low number of nuclei resulted in larger particle sizes. The methyl groups on mesitylamine make the molecule bulkier than the 4-tert-butylbenzonitrile. When both ligands, 4-tert-butylbenzonitrile and mesitylamine, are compared, 4-tert-butylbenzonitrile has a more chain-like geometry. Because of the chain-like geometry of 4-tert-butylbenzonitrile, steric repulsion combined with electrostatic effects had probably prevented the agglomeration of the Ni nanoparticles more effectively, which yielded slightly smaller (3.4 ± 0.9 nm) Ni NPs than at the synthesis with mesitylamine (3.8 ± 0.5 nm). However, the variation in particle size among these syntheses is minimal, making it unreliable to provide a clear explanation.

The results of the above-explained syntheses reveal that the colloidal Ni nanoparticle size could be controlled by changing the ligands during the synthesis. The reducing agent BTB could yield monodisperse Ni NPs. However, the impact of varying the ligand could be further studied by exploring larger molecules because the Ni nanoparticle sizes of syntheses with 4-tert-butylbenzonitrile and mesitylamine were not significantly different.

4.1.3. Effect of different ratios of reactants

The ratios of the reactant were varied during the syntheses to study the effects of the reactants on particle size and particle size distribution. The syntheses were all performed at 90 °C. The reactants were the same in all syntheses, and benzonitrile was chosen as the ligand. Table 1 gives an overview of the syntheses. Ratios are given in mmol and the following order: Ni precursor (Ni)/reducing agent (BTB)/ ligand (benzonitrile). Here on the right is an example of a TEM image of 1.4 nm colloidal Ni NP synthesized with a Ni/BTB/ligand ratio of 1:1:1 is given (Figure 15). The TEM images of the other syntheses are given in Supplementary Information 3 (Figure SI 2 and Figure SI 3).

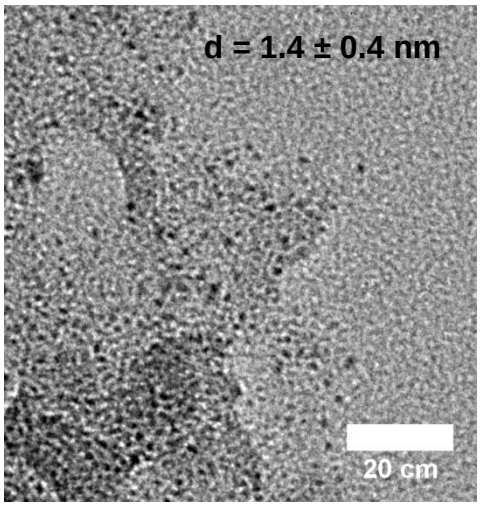

Figure 15 TEM image of 1.4 nm colloidal Ni NP after washing with hexane, synthesized with Ni/BTB/benzonitrile ratio of 1:1:1.

Discussion of the effects of the ratio will be started with the Ni/BTB/benzonitrile of ratio 1:1:1 (Table 1). This ratio gave particles with 1.4 nm size and a standard deviation of 0.4 nm (29.7%). In the following synthesis

(ratio 1:1:3), the ratio of benzonitrile was increased from 1 to 3 mmol, and the ratios of Ni and BTB were held the same at 1 mmol. The change in the benzonitrile ratio gave slightly larger (1.6 nm) NPs, but the standard deviation stayed the same, 0.4 (21.7%).

Table 1 The results of the syntheses with different Ni/BTB/ligand ratios.

Ratio Ni/BTB/Benzonitrile (mmol)	Particle size (nm)	Standard deviation (nm)	Standard deviation (%)
1:1:1	1.4	0.4	29.7
1:1:3	1.6	0.4	21.7
1:3:3	2.1	0.4	17.0
3:3:1	3.2	0.7	21.9
3:1:1	2.5	0.4	16.0
1:3:1	1.5	0.4	22.9
5:5:1	4.0	0.8	21.0

The synthesis with the ratio of 1:3:3 resulted in significantly larger (2.1 nm) Ni NPs, whereby the ratio BTB and benzonitrile were increased to 3. However, the standard deviation, 0.4 (17.0%), stayed the same as in the syntheses with the ratios 1:1:1 and 1:1:3, but more monodisperse Ni NPs were obtained, looking at standard deviation percentages.

Significantly larger NPs (3.2 nm) were yielded after the synthesis with a ratio of 3:3:1 with a higher standard deviation of 0.7 nm (21.9%). The benzonitrile amount was lower than the amount of Ni precursor and reducing agent. A low ligand amount but a higher reducing agent amount resulted in a slightly higher standard deviation. The synthesis with a ratio of 5:5:1 was also performed. Considering these two syntheses, it was confirmed that a high ratio of Ni precursor and BTB negatively affects particle size distribution due to ongoing homogenous nucleation, compared to a high ratio of Ni precursor with a low ratio ligand amount (ratio 3:1:1).

The expectation for the synthesis with the ratio 3:1:1 was to obtain much larger NPs than 3.2 nm (ratio 3:3:1) because of the low ratio reducing agent. However, the ratio of 3:1:1 led to NPs with a size of 2.5 nm and a standard deviation of 0.4 nm (16.0). They were significantly smaller than 3.2 nm. An explanation is that ongoing homogenous nucleation did not happen during the synthesis. This can be seen in the standard deviation value, which was lower than in the synthesis with a ratio of 3:3:1 (21.9%). Another explanation could also mean that a part of the Ni^{2+} was not reduced due to less reducing agent, meaning an excess of Ni precursor in the solution. This excess of Ni precursor was also observed from the green color of the hexane waste after the washing.

The synthesis with the ratio of 1:3:1, where only the ratio of BTB was increased (3 mmol), and the ratio of other reactants stayed low (1 mmol), resulted in Ni NPs of 1.5 nm particle size with a standard deviation of 0.4 nm (22.9%). The change in particle size was not significantly larger than the synthesis with the ratio 1:1:1.

In the end, changing the ratios of the reactants resulted in different particle sizes. The size distribution of the particles was strongly affected by the ratio of BTB and the second reactant. Changing the BTB ratio alone did not affect the particle sizes and dispersion. Hereby, the amount of the Ni precursor was crucial in determining the particle size. The data of syntheses with the ratios 1:1:3, 3:1:1 and 1:3:1, whereby the amount of only one reactant was increased, had shown that the particle size increased significantly when the amount of Ni precursor was increased (ratio 3:1:1). This phenomenon was in line with the mentioned nucleation theory. A large amount of Ni precursor results in a small ΔGv value because of the increase of the molar volume of solid (v), which lead to a larger critical nucleus radius. Figure 16 shows that when a higher ratio of BTB and Ni precursor was used against the ligand ratio (3:3:1 and 5:5:1), the synthesis gave larger Ni NPs with broader size distribution. The desired result was changing the particle size with a narrow size distribution. Therefore, the optimum ratio for the synthesis of Ni NPs could be chosen as 1:3:3 because the standard deviation (%) was one of the lowest among the different ratios and no metal precursor was in excess in the solution. The discussion will be followed by the synthesis of different colloidal metal nanoparticles by applying our synthesis method for colloidal Ni nanoparticles.

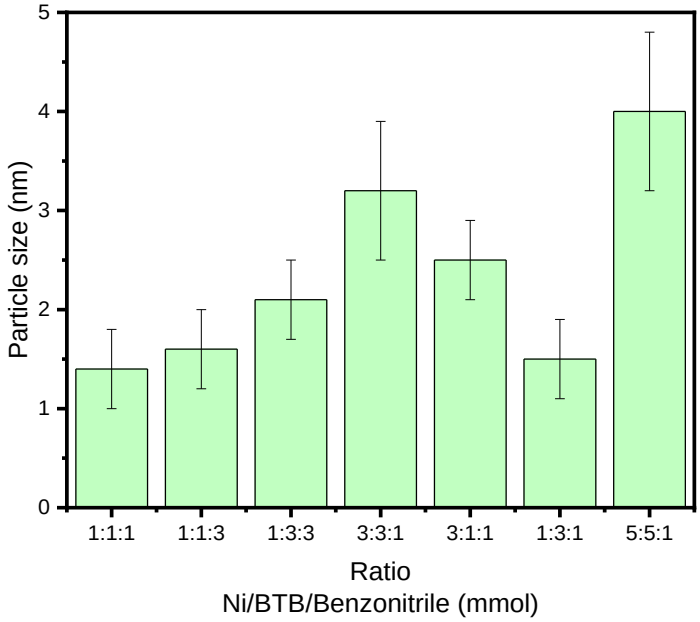

Figure 16 The particle size of the synthesized Ni NPs is plotted versus Ni/BTB/ligand ratios used with standard deviations, given with green column bar.

4.2.Synthesis of various metal nanoparticles

The above-described colloidal synthesis method for Ni NPs was performed with different metal precursors. With these performed syntheses, it was aimed to confirm the versatile applicability of this colloidal synthesis method for other metal NPs than Ni NP. The conditions were the same during these syntheses, except the metal precursors were changed. The reaction temperature was held at 90 °C, mesitylamine was chosen as the ligand, and the ratios of Ni/BTB/mesitylamine were 1:3:3. The motivation for mesitylamine as a ligand was that data was already available on the cobalt synthesis with mesitylamine. The metal precursors were manganese(II)acetylacetonate, iron(III)acetylacetonate, cobalt(II)acetylacetonate, nickel (II)acetylacetonate, copper(II)acetylacetonate and ruthenium(III)acetylacetonate. Ruthenium is a 4d-transition metal, and the other metals are 3d-transition metals. The reaction products were washed with hexane using the same method for washing colloidal Ni NPs. Table 2 gives an overview of the results of the syntheses, with atomic numbers, overall reactions and standard electron potential, which tells how likely the metal ion is to be reduced. A metal ion with a negative reduction

potential has a high electron-donating capacity and is therefore highly reducing. On the other hand, a metal ion with a positive reduction potential has a high electron-accepting capacity and is therefore highly oxidizing.

Table 2 The results of the syntheses with different metals with their atomic number and electron potential.[43]

Atomic number	Metal ions	Particle size (nm)	Standard deviation (nm)	Standard deviation (%)	Overal reaction	Electron potential (V)
25	Manganese (II)	3.4	0.6	17.6	$Mn^{2+} + 2e^- \rightleftharpoons Mn$ (s)	- 1.180
26	Iron (III)	6.8	1.6	23.5	$Fe^{3+} + 3e^- \rightleftharpoons Fe$ (s)	- 0.037
27	Cobalt (II)	2.0	0.4	19.5	$Co^{2+} + 2e^- \rightleftharpoons Co$ (s)	- 0.277
28	Nickel (II)	3.8	0.5	13.7	$Ni^{2+} + 2e^- \rightleftharpoons Ni$ (s)	- 0.250
29	Copper (II)	1.4	0.3	21.4	$Cu^{2+} + 2e^- \rightleftharpoons Cu$ (s)	+0.337
44	Ruthenium (III)	8.1	1.4	17.0	$Ru^{3+} + 3e^- \rightleftharpoons Ru$ (s)	+0.600

During the synthesis of Mn NPs, the reactants were not entirely dissolved in the toluene solution at 90 °C. The color of the solution did not change for a while after the injection of BTB, the reducing agent. Finally, the reaction temperature was increased to 100 °C to force the start of nucleation. The reactants were dissolved entirely, and the solution color changed from cream to light-brown color. The synthesis of Fe NPs started by completely dissolving the reactants between 80 – 90 °C, and a dark-red solution was obtained. The color did not change after the injection of the reducing agent. In the case of Cu NPs synthesis, the reactants were not dissolved, even heated up to 100 °C. The injection of BTB resulted in a solution with large black particles on the bottom of the flask. The color of the solution became transparent at the end of the reaction.

A decrease was visible in particle sizes from 3d-metal Mn NPs (3.4 nm, Figure 17a) to Cu NPs (1.4 nm, Figure 17b), except Fe (Figure 18a) and Ni NPs (Figure 14a). This decrease was related to the standard reduction potentials (last column in Table 2). In Figure 18d, the particle sizes are plotted against the reduction potential of the metal ions. So, manganese has the lowest potential, with the largest particle size. On the other hand, copper has the highest reduction potential among the 3d-transition metals, with the smallest particle size. It means that the degree of reducibility difficulty increases from Cu to Mn ions. The reduction of Cu will take place faster than those of Mn. It leads

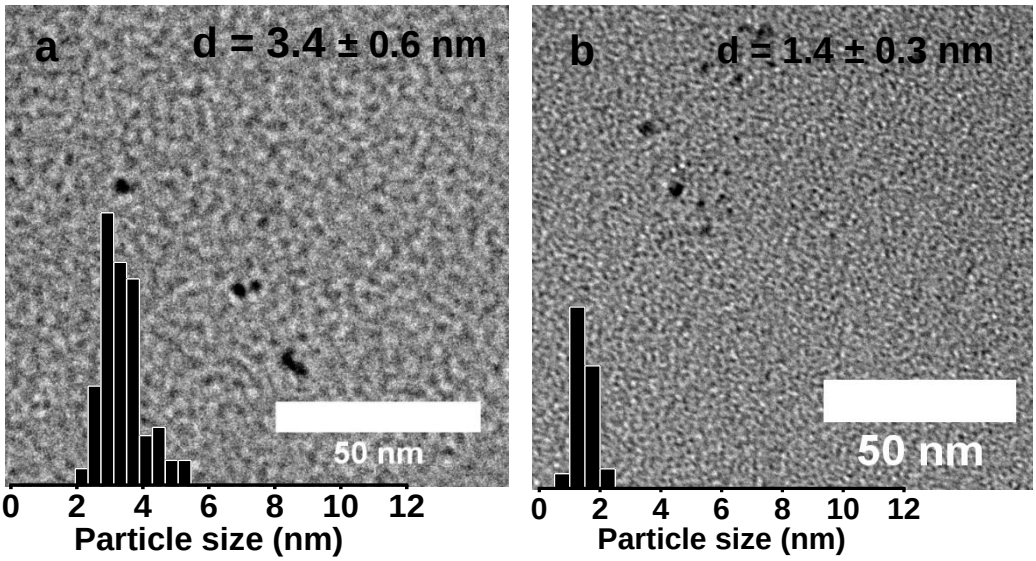

Figure 17 TEM images of (a) 3.4 nm colloidal Mn NPs and (b) 1.4 nm colloidal Cu NPs after washing with hexane, synthesized with the colloidal synthesis method developed for colloidal Ni NPs.

to smaller Cu NPs and larger Mn NPs. Ni NP (3.8 nm) was the outlier in the decreasing trend. Furthermore, there was also a relation between atomic weights and particle size among the 3d-transition metals. Larger atoms gave smaller NPs after the synthesis, except Ru and Fe NPs.

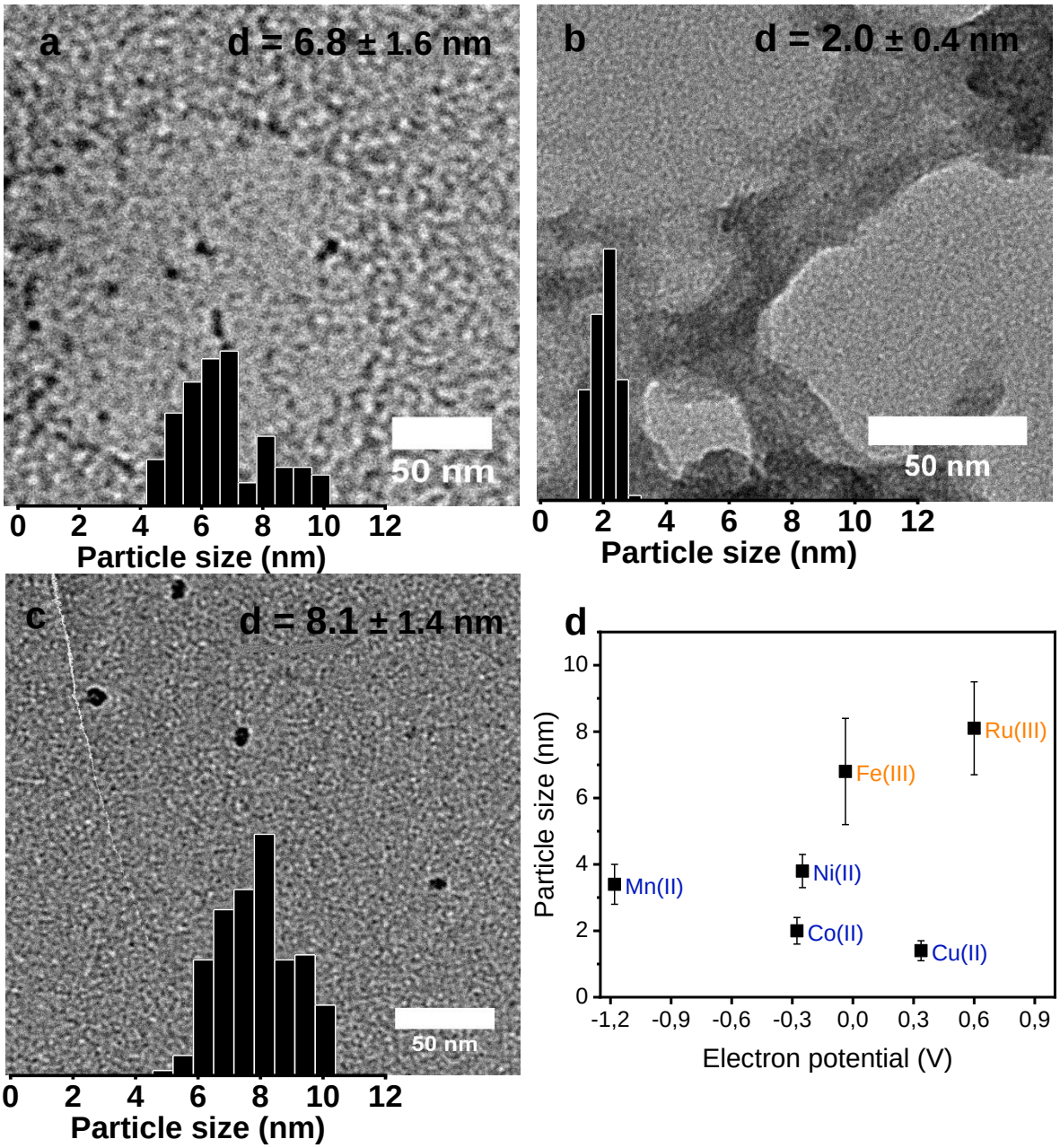

Figure 18 TEM images of the different colloidal metal NPs after washing with hexane: a) 6.8 nm Fe NPs, b) 2.0 nm Co NPs (By Bram Kappé, with permission) and c) 8.1 nm Ru NPs. (d) The particle sizes of different colloidal metal nanoparticles plotted versus reduction potential of the metal ions.

The large Fe NPs (6.8 nm) were caused by the 3^+ charge of the iron ion from the metal complex. This also applies to Ru NPs (8.1 nm, Figure 18c). Ruthenium ($[Kr]4d^5 \rightarrow [Kr]4d^7\ 5s^1$) and iron ($[Ar]3d^5 \rightarrow [Ar]3d^6\ 4s^2$) ions needed more electrons from the reducing agent to be reduced. The third electron was needed to fill the d-band of the corresponding metal ion. In the case of the 2+ metals, only the 4s orbital was filled. Therefore, reducing Fe and Ru ions took more time than reducing 2+ ions, and the critical radius was reached slowly to form a stable nucleus. Slowly reducing resulted in fewer nuclei numbers and larger nanoparticle sizes in the solution.

In the end, different colloidal metal NPs were synthesized by applying the method for the synthesis of colloidal Ni NPs. However, some steps of the synthesis method could be optimized. For example, washing the reaction product could be done by trying other solvents. In Figure 18b with Co NPs, there were still a significant amount of organic compounds present in the sample. Co NP samples could be washed properly to get cleaner TEM images. Another example is using a stronger reducing agent for the reduction of Fe^{3+} and Ru^{3+} than BTB. This will result in more monodisperse NPs. Instead of changing the reducing agent, the choice of precursor could also be changed to 2+ metals (Fe^{2+}) instead of 3+ metals. Then, the data of all metal nanoparticle syntheses could be compared more consistently.

Summarising the synthesis of colloidal nanoparticles part, a colloidal synthesis method was shown to prepare Ni nanoparticles with different sizes between 1.4 and 6.6 nm. The particle sizes of colloidal Ni NPs were tuned by selecting different reaction temperatures, ligands and ratios of the reactants. Significantly larger particles were obtained when the reaction temperature was drastically decreased. Using bulkier ligands resulted in larger nanoparticles compared to the smaller ligands. Changing the ratios made it clear that the Ni precursor amount played a crucial role in determining the particle sizes. Besides, the reducing agent BTB could be considered the main reactant responsible for the particle size distribution. Higher reaction temperature (90 °C), smaller ligands with reactive functional groups (benzonitrile) and a low ratio of Ni precursor and together with a high ratio of BTB (1:3:3) will result in Ni NPs with a very narrow size distribution. It was also shown that this colloidal synthesis method for Ni NPs works for preparing other colloidal metal nanoparticles (Mn, Fe, Cu, Co, Ru).

The discussion will be followed by a discussion of the intermediate steps forward to the catalytic activity experiments of the colloidal Ni NPs during CO_2 hydrogenation catalysis. Firstly, the deposition of colloidal Ni NPs onto silica support will be discussed, followed by the discussion of the ligand removal using Meerwein's reagent. After that, the results of catalytic activity experiments of five samples with different Ni nanoparticle sizes ranging from 1.4 to 6.6 nm will be shown.

4.3.Deposition of Ni NPs on the silica support

The colloidal Ni NPs were deposited on silica to use in catalytic activity experiments. The deposition was performed in the glove box. First, Ni NPs and silica were dissolved in toluene separately in two vials. The mixture was stirred for 30 minutes after adding Ni NPs to the silica toluene solution. After stirring, the solvents were removed. The Ni/SiO_2 product was washed twice with THF or hexane, depending on if the ligand removal was applied. The intended Ni weight loading was 2.5 wt.%. The actual Ni weight loadings were afterwards determined with AAS. The calculations are included in Supplementary Information 4.

The Ni/SiO_2 and Meerwein's reagent (Mw) treated products were washed outside the glove box during the first deposition experiments. Washing the NiNP4.4@SiO_2Mw sample outside the glove box resulted in at least five times lower Ni weight loading (0.10 wt.% Ni) on silica than at washing NiNP2.8@SiO_2Mw sample (0.64 wt.% Ni) inside the glove box (Figure 19). However, this low Ni loading was not found in every sample when washed outside the glove box. For example, the Ni loading in the sample NiNP1.9@SiO_2Mw was higher (0.48 wt.% Ni) than the Ni loading in NiNP4.4@SiO_2Mw sample (0.10 % Ni), while both samples were washed outside the glove box. Possibly, smaller Ni NPs adhered better than larger particles on silica.

The lower Ni loading could be explained by the fact that Ni NPs on silica oxidized faster outside the glove box in the atmosphere. As a result, Ni NPs may be detached from the silica and quickly washed away with washing solvent, resulting in lower Ni loading of the samples. Therefore, it was decided to always wash the Ni/SiO_2 products in the glove box to avoid these issues. The deposition of Ni NPs on silica was followed by the ligand removal step, which will be covered in the following section.

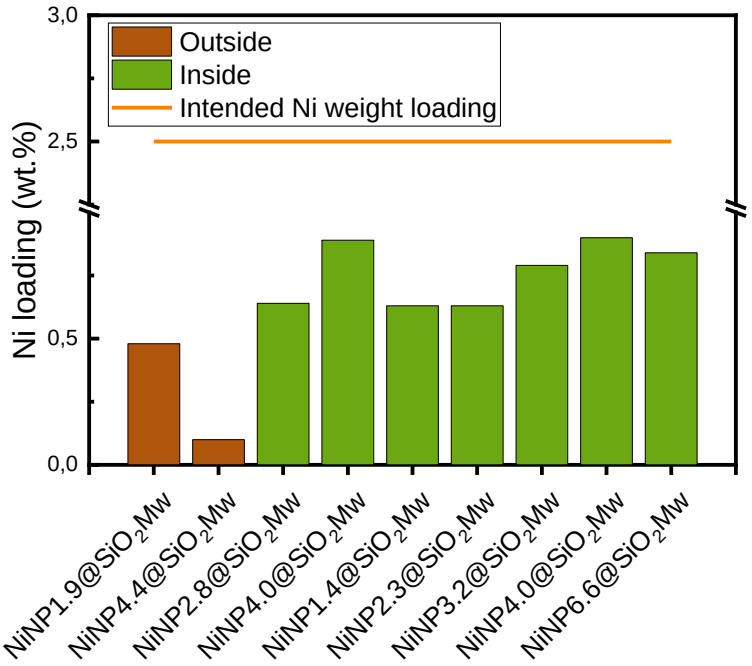

Figure 19 Ni loadings of the prepared samples are shown with the washing step inside and outside the glove box with column bar. Samples were washed inside the glove box after that NiNP2.8@SiO_2Mw sample showed higher Ni loading. The orange line gives the intended Ni weight loading.

4.4.Ligand removal

Before the catalytic activity experiments, the ligands should be removed from the colloidal Ni NPs. Meerwein's reagent in acetonitrile, to remove the ligands, was added to the solution of Ni NPs and silica in toluene after the deposition step. After stirring for an hour, solvents were removed and the product was washed twice with THF in the glove box. The process is given in Scheme 2. The removal of the ligands (Scheme 2, green i) was based on the method from Rosen *et al*. They reported that Meerwein's reagent acted as a universal class of ligand stripping reagent thanks to its strong alkylating character.[49] The interaction ii and iii give the possible other interactions. Meerwein's reagent can also alkylate the Ni NP and the silica surface.

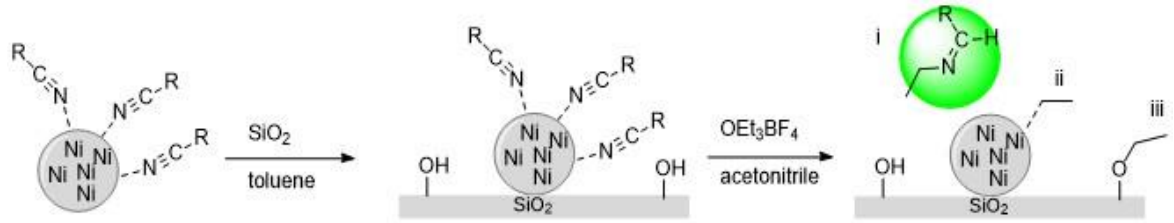

Scheme 2 Deposition of Ni NPs on SiO_2 support and the removal of the benzonitrile ligand with possible interactions (i-iii) of the ethyl groups from Meerwein's reagent with OH groups on SiO_2 surface.

In order to follow the changes in the ligand's presence during calcination experiments, operando DRIFTS was used. The DRIFTS spectra of the samples after Meerwein's reagent treatment were compared with the spectra of the sample without Meerwein's reagent to investigate the removal technique. The FT-IR spectra of the samples NiNP(PhCN)1.9@SiO_2 and NiNP(PhCN)1.9@SiO_2Mw during the calcination experiments are given in Figure 20. The calcination experiments were performed to form the nickel metal into a nickel oxide. More importantly, it was performed to follow the changes in the IR bands of the ligands while the temperature increased gradually. The samples were heated to 400 °C with a flow of O_2 and the IR spectra were measured using an operando FT-IR spectroscopy.

The weak band at 2185 cm^{-1} belongs to CN stretching vibrations from the benzonitrile ligand. The negative absorption band at 2300 cm^{-1} is due to the difference in CO_2 flow between the background and the sample. The background spectrum was taken at room temperature in the air. The broad band around 2931 cm-1 represents C-H stretching vibrations, probably from the ethyl groups of the reducing agent (BTB) and residual solvent. The two peaks around 3040 cm^{-1} indicate the C-H stretching vibrations of the aromatic ring from the benzonitrile ligand. Furthermore, the

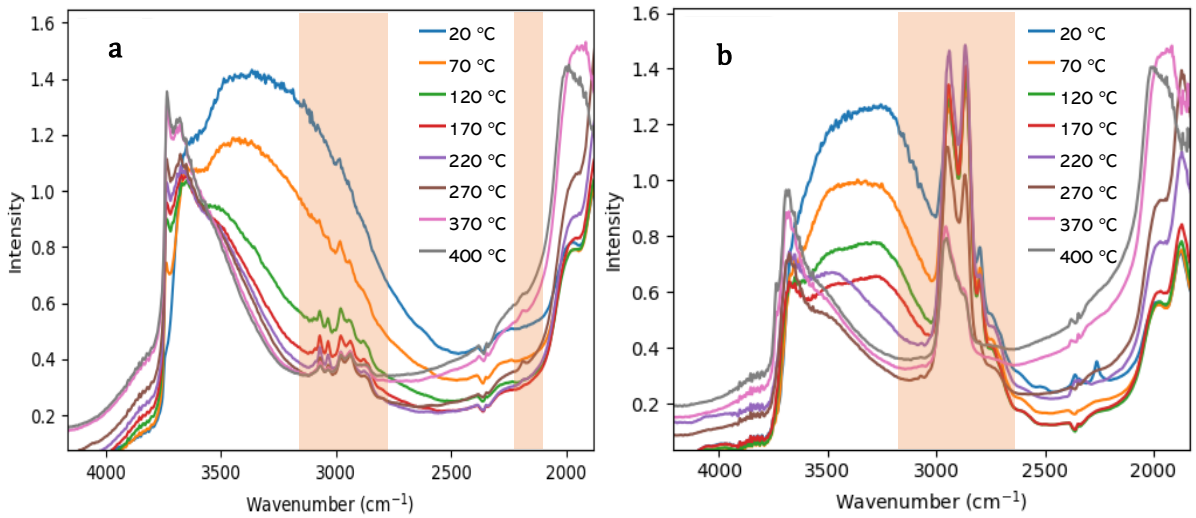

Figure 20 DRIFTS spectra of the samples (a) NiNP(PhCN)1.9@SiO_2 and (b) NiNP(PhCN)1.9@SiO_2Mw during calcination experiments, heated to 400 C in O_2 flow.

band at 3742 cm^{-1} belongs to O-H stretching vibrations, available on the SiO_2 surface. The broadband between 3500 and 3000 cm^{-1} is the O-H stretching band from water. This band is not present anymore in the sample after heating the sample. Figure 20a shows the presence of benzonitrile ligands (3040 cm^{-1}) in sample NiNP(PhCN)1.9@SiO_2 sample before the treatment with Meerwein's reagent.

Figure 20b gives the FT-IR spectra of sample NiNP1.9@SiO_2Mw treated with Meerwein's reagent. The most important differences between the two spectra are the bands of the CN group and the aromatic C-H bond, which disappeared in Figure 20b. Disappearing these two bands indicates the removal of the benzonitrile ligand using Meerwein's reagent. However, there are broad peaks appeared between 2750 and 3000 cm^{-1}. This strong band belongs to the C-H stretching vibrations, resulting from the C-H bonds of ethyl groups of Meerwein's reagent.

Although, as mentioned at the beginning of this section, there were also other possible interactions between the Ni NP and ethyl groups, and OH groups on the silica and ethyl groups from Meerwein's reagent, shown in Scheme 2(i-iii). Removal of the benzonitrile ligand proves interaction i had occurred. Otherwise, the benzonitrile ligand would not be removed from the Ni NPs and would still be visible in the spectrum. This formed intermediate imine was then washed out with the THF. The probability of ii would be low because of the lack of functional groups on both Ni NP surface and ethyl groups. Interaction iii will most likely happen because of the basic OH groups on the SiO_2 surface. Additionally, the concentration of OH groups in the solution was high due to the SiO_2 amount in the solution. This explains the strong absorbance of the with ethyl groups coupled OH groups on the SiO_2 surface.

4.4.1. Removal of the ethyl groups

The above-discussed strong ethyl groups are undesirable in a supported catalyst and also not desired during its characterization measurements. Therefore, it was aimed to remove the ethyl groups from the SiO_2 surface, which were responsible for the strong absorbance between 2750 and 3000 cm^{-1}. After several unsuccessful attempts to remove these ethyl groups using NH_3 solution and other techniques (Supplementary Information 5), the reduction of the catalyst samples was found as a successful method to remove the ethyl groups. The reduction experiments with N_2/H_2 flow using operando FT-IR were performed on NiNP@SiO_2Mw samples without treating them with NH_3 solution. In most cases, the ethyl groups were completely removed during the reduction experiments (Figure 21c and d). Probably, ethyl groups were hydrogenated to form

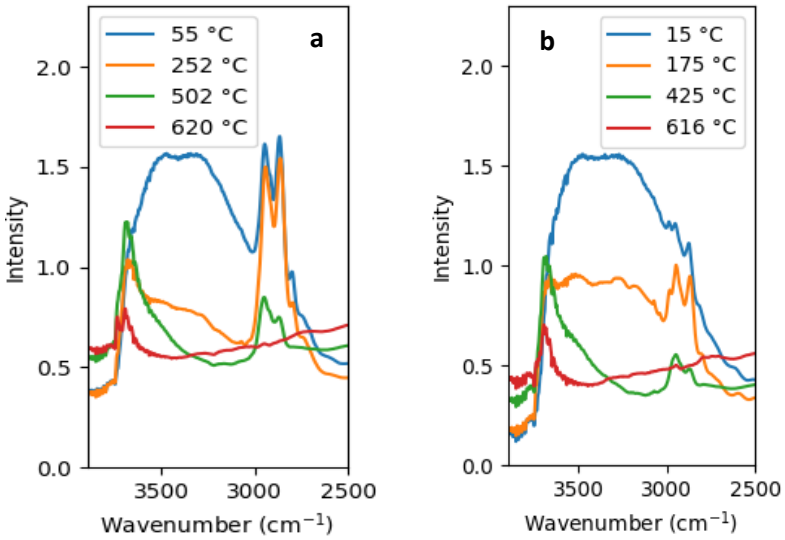

Figure 21 DRIFTS spectra of (a) NiNP1.4@SiO_2Mw sample and (b) NiNP3.2@SiO_2Mw sample during the reduction (N_2/H_2, 540 °C) experiments .

ethane. Furthermore, these ethyl groups can affect the CO_2 hydrogenation experiments by being the source for carbon atoms in methane formation. The effect of the ethyl groups was studied during the CO_2 hydrogenation experiments by adapting the experiment's condition. Their presence in the catalysts could affect the catalysis, which will be discussed in section 4.5.

Finally, we can conclude that the ligands were removed using Meerwein's reagent. During the ligand removal step, the ethyl groups from Meerwein's reagent alkylated the SiO_2 surface. A couple of techniques were carried out to remove these ethyl groups from the support surface. Reduction of the samples in N_2/H_2 flow was found as a working method. After selecting the ligand removal method, five catalysts with different Ni nanoparticle sizes were prepared for structure sensitivity CO_2 hydrogenation experiments. The results of the CO_2 hydrogenation experiments will be discussed in the next Catalytic activity section.

4.5.Catalytic activity experiments

The activity of colloidal Ni NPs was determined by measuring the FT-IR spectra of supported Ni/SiO_2 catalysts (Figure 23a, b) using operando DRIFTS spectroscopy during CO_2 hydrogenation experiments. The samples were prepared (A-G) by following the discussed preparation method before this section. Sample H was a commercially available BASF catalyst with 2.1 ± 1.1 nm Ni NPs. An overview of the samples with used ligands, reaction temperature, ligands, particle sizes and Ni weight loading is given in Table 3.

The CO_2 hydrogenation experiments were started after reducing the sample in a flow of N_2/H_2. The samples were reduced for one hour at 620 °C before being cooled to 200 °C. The set temperature of 620 °C was an extern temperature, which strongly differs from the actual temperature of the bed. Calibration measurements (standard conditions) with an external thermocouple showed that 620 °C corresponds to approximately 540 °C actual temperature in the cell. After that, CO_2 hydrogenation was started by heating the sample from 200 °C to 400 °C with a flow of CO_2/H_2 (1/4). The CO_2 hydrogenation step was also held for one hour at 400 °C.

Table 3 The overview of the samples used during the CO_2 hydrogenation experiments.

	Sample	Temperature (°C)	Ratio (Ni/BTB/ligand)	Particle size (nm)	Standard deviation (nm)	Standard deviation (%)	Ni loading (wt%)
A	NiNP1.4@SiO_2Mw	90	1:1:1	1.4	0.4	29.7	0.63
B	NiNP2.3@SiO_2Mw	90	1:3:3	2.3	0.4	17.0	0.79
C	NiNP3.2@SiO_2Mw	90	3:3:1	3.2	0.7	21.9	0.63
D	NiNP4.0@SiO_2Mw	90	5:5:1	4.0	0.8	21.0	0.90
E	NiNP6.6@SiO_2Mw	50	1:3:3	6.6	1.1	16.7	0.84
F	NiNP(PhCN)1.4@SiO_2	90	1:1:1	1.4	0.4	29.7	0.63
G	NiNP(PhCN)4.0@SiO_2	90	5:5:1	4.0	0.8	21.0	0.68
H	BASF	-	-	2.1	1.1	-	11.8

The reduction temperature for the reduction experiments was determined by Temperature Programmed Reduction (TPR) analysis. TPR of samples A and E were measured and the data are shown in Figure 22. The peaks around 500 °C were attributed to the reduction of nickel oxide particles on the silica support. The peaks at 250 °C and 400 °C could be attributed to the ethyl groups because the samples still contain the ethyl groups on the silica surface.

Also, the peak of nickel oxide in sample NiNP6.6@SiO_2Mw is shifted to a higher temperature when compared with the peak of the NiNP1.4@SiO_2Mw sample. The difference in particle size could cause this shift. Vogt *et al.*[21] reported that smaller supported Ni NPs were reduced at a higher temperature than supported larger Ni NPs but Figure 22 shows an opposite trend. However, it is necessary to measure the reduction temperature for other samples (B-D) with different particle sizes to explore this trend. Additionally, the measurements could be expanded with TGA-MS to follow the changes in the sample. TGA-MS will help to assign the peaks to the compounds.

Based on these TPR profiles, the reduction temperature for the catalytic activity experiments was set at 550 °C. After that, operando FT-IR spectroscopy experiments were performed. The discussion will further focus on the catalytic activity of the samples, which will be followed by the discussion of reaction intermediates.

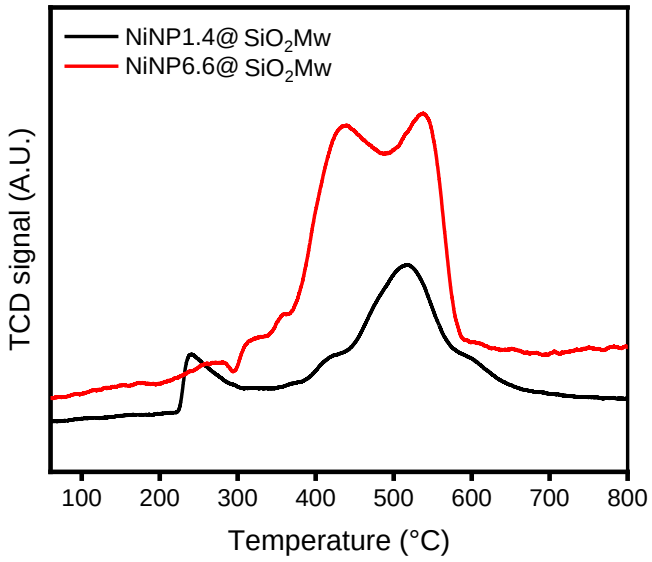

Figure 22 H_2-TPR profiles of NiNP1.4@SiO_2Mw and NiNP6.6@SiO_2Mw samples.

4.5.1. Catalytic activity estimations

Operando spectroscopy was performed with these (A-G) samples to study the relation of particle size with catalytic activity. The subtracted spectra are used to discuss the catalytic activity of the samples, as shown in Figure 23a (sample A). These subtracted spectra were obtained by subtracting the spectrum of the silica at the same temperature during the cooling step before the hydrogenation step from the raw spectra of the samples during the CO_2 hydrogenation step.

To calculate the activity, the following procedure was used. First, the area of the methane band between 3007 and 3027 cm^{-1} was integrated (Figure 23b). Then, the amount of Ni NPs in the sample was calculated using Ni weight loading from AAS analysis and measured particle sizes. Ni NP surface area was then calculated using the amount of Ni NPs in the sample according to the formulas of the sphere volume. At last, the mol of Ni on the surface was calculated by assuming 10 Ni atoms/nm^2 in arbitrary units and plotted versus particle size. The formulae for the calculations are given in Supplementary Information 6. Finally, the average values of the last 30 spectra were taken to compare the activity of the samples, given in Figure 24b.

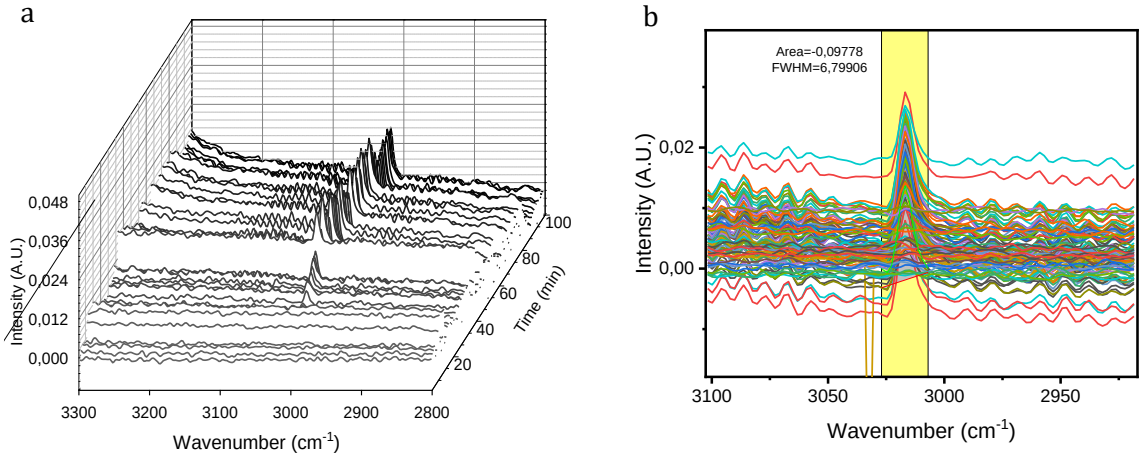

Figure 23 (a) Operando FT-IR spectra of sample NiNP1.4@SiO_2Mw (A) during the CO_2 hydrogenation experiment (temperature 200-400 °C, ramp: 5 °C/min, H_2/CO_2 flow: 16/4 ml/min) between the region 3300-2800 cm^{-1} for methane band. (b)The integrated region of the methane band between 3007 and 3027 cm^{-1} for catalytic activity calculations

Usually, the mean particle sizes after reduction were used for the activity calculations in the works of Vogt *et al.*,[1,21] but here, the mean particle sizes of the colloidal Ni NPs were used. An accurate determination of the particle sizes after reduction needed high-resolution TEM equipment, which was not feasible to use within the time. Although, a number of the spent samples were measured for their particle sizes using the TEM Technai 20. The samples were prepared by crushing and dispersing them in ethanol. The TEM images of the samples indicated that particles were maybe grown after CO_2 hydrogenation experiments. For example, Ni NPs in sample NiNP3.2@SiO_2Mw (C) were grown from 3.2 $\pm$ 0.7 nm to 6.5 $\pm$ 1.1 nm after the CO_2 hydrogenation experiment (Supplementary Information 7, Figure SI 7). However, these TEM Technai 20 images of the spent catalysts were not reliable enough evidence to conclude the particle growth because detecting the Ni NPs on silica support was not possible due to the low resolution of TEM Technai 20. Figure SI 7 shows separate black particles without visible silica support, which could also be some contaminations in the sample. Although there were indications of particle growth, it was assumed, for the catalytic activity calculations, that particles were not grown due to the lack of information about the particle growth during the CO_2 hydrogenation catalysis. This means that the reported catalytic activity results can change in the future when the particle sizes are measured in the spent samples.

At this moment, it is unknown during which step these Ni NPs were grown if they grew. They could grow during the reduction and CO_2 hydrogenation steps, but the reduction step will play a more significant role here than the hydrogenation step. This particle growth was probably due to the high temperature during the reduction step, which could cause the sintering of the Ni NPs, as indicated in the work of Terreni *et al.*[31] The used gasses during CO_2 hydrogenation could also have a role in particle growth. An alternative technique could be in situ XRD measurements to follow the particle growth during CO_2 hydrogenation.

Figure 24a shows that Meerwein's treated Ni/SiO_2 samples were active during the CO_2 hydrogenation reaction to form methane. Methane formation in all samples confirms that the ligand removal technique using Meerwein's reagent works for this colloidal approach.

Since it was known from the FT-IR spectra of ligand removal that the ethyl groups had alkylated the silica surface, uncertainty can exist about the origin of carbon atoms for methane formation. Therefore, the CO_2 flow was turned off during the CO_2 hydrogenation experiment with sample NiNP2.3@SiO_2Mw (B) to confirm that the carbon atoms originate from the CO_2 gas. As seen in Figure 24a, the activity of sample NiNP2.3@SiO_2Mw (B) stopped immediately after turning off the CO_2 flow for 20 minutes between 46 and 66 minutes. When the CO_2 gas flowed again, the activity level became the same as before turning off. Thanks to this change in the experiment, it can be concluded that ethyl groups on the silica surface were not participating in the CO_2 hydrogenation experiment. However, the chance for coke formation from ethyl groups is not excluded, which could be studied in the future using Raman spectroscopy by analyzing the spent samples.

Also, from the CO_2 turn-off experiment (sample B), it can be concluded that the baseline is not zero. Therefore, the activities were recalculated using the peak integration of the CO_2 turn-off experiment region (45-65 minutes) as a baseline for all the samples to reduce the error to the minimum (Figure 24a). However, the baselines for each sample must be acquired in the future. Here, the main difference is in samples D and E activity when the activities are compared without baseline corrected, non-normalized plots (Supplementary Information 8, Figure SI 8). By applying the baseline correction, the activity values of both samples changed their position. Sample NiNP4.0@SiO_2Mw (D) showed more activity than sample NiNP6.6@SiO_2Mw (E).

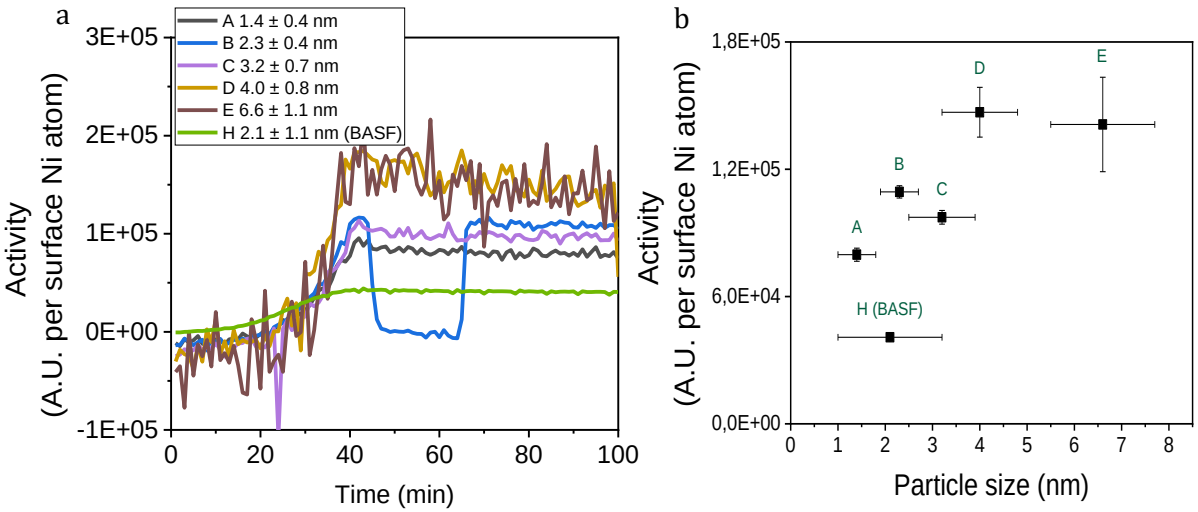

Figure 24 a) Recalculated methane activity of samples A-H using a baseline from CO_2 turning off experiment, from the CO_2 hydrogenation experiments (temperature 200-400 °C, ramp: 5 °C/min, H_2/CO_2 flow: 16/4 ml/min), b) the particle size effect on activity in A.U. per surface Ni atom.

The activity of a commercially available BASF catalyst (sample H) was tested to compare the activity of colloidal Ni NPs in a similar way instead of TOF values, which were not calculated in this study due to the absence of GC data. The activity of sample H was calculated with the same method (Figure 24a and b). Sample H with 2.1 ± 1.1 nm Ni NPs had lower catalytic activity than synthesized colloidal Ni catalysts. This comparison shows that colloidal Ni catalysts were highly active in the CO_2 hydrogenation experiments.

As previously discussed in the Catalytic activity 2.2, the Ni NPs with particle size around 2.5 nm for Ni/SiO_2 prepared by HDP were the most active in the CO_2 hydrogenation experiments compared to the other particle sizes (Figure 24c). Therefore, the expectation was to get an activity trend with a maximum activity for sample NiNP2.3@SiO_2Mw (B), as shown in Sterk *et al.* (Figure 24d).[2] Interestingly, the activity trend in Figure 24b is not entirely in line with the computational and experimental data.[2,21] The trend between samples A-C is in line, but the activity of samples D and E are not in line. Samples D and E were expected to have lower activity than sample NiNP2.3@SiO_2Mw (B). This activity trend refers to the activity trend of undercoordinated atoms in Sterk *et al.*[2] The blue line with undercoordinated atoms shows no maximum activity around 2.5 nm particle size.[2] Meaning is that the colloidal Ni NPs probably contain less undercoordinated and defect sites when compared with BASF catalyst (sample H).

Furthermore, samples F and G, not treated with Meerwein's reagent, were also tested for their activity. Their activities were compared with the results of samples A and D, and they are shown in Figure 25. Herein, the difference between samples A and F is clear. Sample NiNP(PhCN)1.4@SiO_2 (F) still had ligands during the CO_2 hydrogenation experiments, which blocked the working of Ni catalysts during the reactions, while sample NiNP1.4@SiO_2Mw (A) was treated with Meerwein's reagent to remove the ligands making the Ni catalysts active in the CO_2 experiments.

However, this same difference is not visible between samples NiNP4.0@SiO_2Mw (D) and NiNP4.0@SiO_2Mw (G). Approximately the same activity values are seen for samples D and G (Figure 25), which was not the expectation. Sample G should not be active in the CO_2

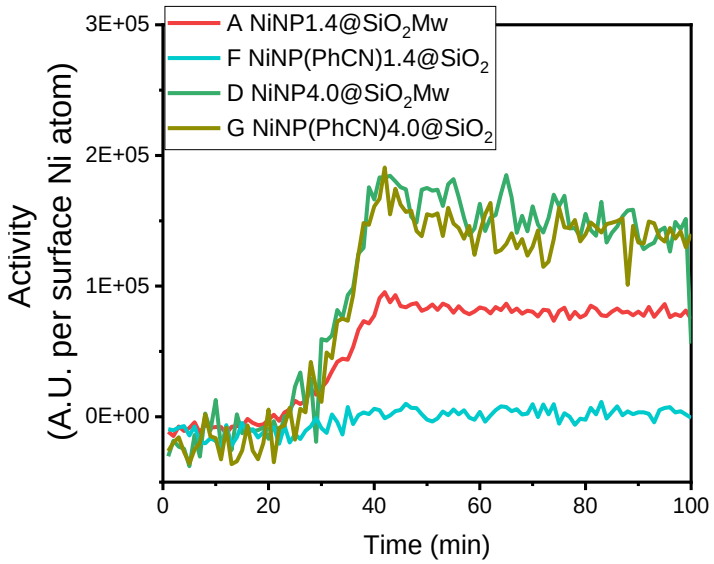

Figure 25 Recalculated methane activity of samples A, F, D and G using a baseline from CO_2 turning off experiment (Sample B), from the CO_2 hydrogenation experiments (temperature 200-400 °C, ramp: 5 °C/min, H_2/CO_2 flow: 16/4 ml/min). The activity (A.U. per surface Ni atom) of Meerwein's reagent-treated samples (A and D) compared with the untreated samples (F and G). Sample F is the untreated catalyst with the same colloidal Ni NPs as in sample A. Sample G is the untreated catalyst with the same colloidal Ni NPs as in sample D. Samples A and F showed different methane activity, while samples D and G showed almost the same methane activity.

hydrogenation experiments because of the ligand presence. However, the first raw FT-IR spectra of sample NiNP4.0@SiO_2Mw (D) showed that the ligands were not entirely removed after Meerwein's reagent treatment. This partial removal of the ligands can be an indication that the ligand removal method with Meerwein's reagent was probably not effective enough to remove all the ligands with larger Ni NPs. Therefore, Meerwein's reagent ligand removal procedure should be modified for larger NPs. For example, it can be changed by increasing the amount of Meerwein's reagent. The activity of sample D could be measured more reasonably if the ligands were removed better.

In addition, the high activity of sample NiNP(PhCN)4.0@SiO_2 (G) could also mean that larger Ni NPs in the presence of ligands are more active than smaller Ni NPs with ligands. To confirm this hypothesis, the activity of samples B, C and E before Meerwein's reagent treatment should also be calculated to have more data to draw clear conclusions about the ligand effects on the catalytic activity.

In summary, Meerwein's reagent-treated, silica-supported colloidal Ni NPs were active during CO_2 hydrogenation catalysis. They also showed higher activity than a commercial BASF catalyst. However, a characteristic and optimum activity could not be seen for the colloidal Ni NPs around 2.5 nm particle size, as reported in the literature for silica-supported Ni NPs prepared by HDP.[1,2] To explore the CO_2 hydrogenation catalysis, the reaction intermediates of CO_2 hydrogenation reaction with their FT-IR absorbance bands will be discussed, and a conclusion will follow in the following section.

4.5.2. Reaction intermediates

The reaction intermediates could be seen in the subtracted FT-IR spectra of samples between 1700 and 2250 cm^{-1}. An example is given in Figure 26 for sample A. Figure 27 shows the region of interest region for the intermediates and methane band of samples A-E before, at the start and at the end of CO_2 hydrogenation catalysis. The bands between 1700-1980 cm^{-1} belong to bridged or three-fold carbonyl C=O stretching vibrations. Here, the noise makes the peaks not clear enough to assign them. To be precise, the peak at 1930 cm^{-1} was attributed to these carbonyl vibrations, thanks to the study of Vogt *et al.*[21] The prominent peak around 2050 cm^{-1} was attributed to the absorbed CO on a single Ni atom. The peaks at 2177 cm^{-1} and 2050 cm^{-1} were assigned to gaseous CO. The peak of gaseous CO is not visible at 2050 cm^{-1} due to the stronger absorbance of CO_{ads} (top). At last, the methane peak appeared at 3015 cm^{-1}. Below 1700 cm^{-1}, the absorption of silica support was too strong, which made the assigning of formate band challenging. Therefore, the

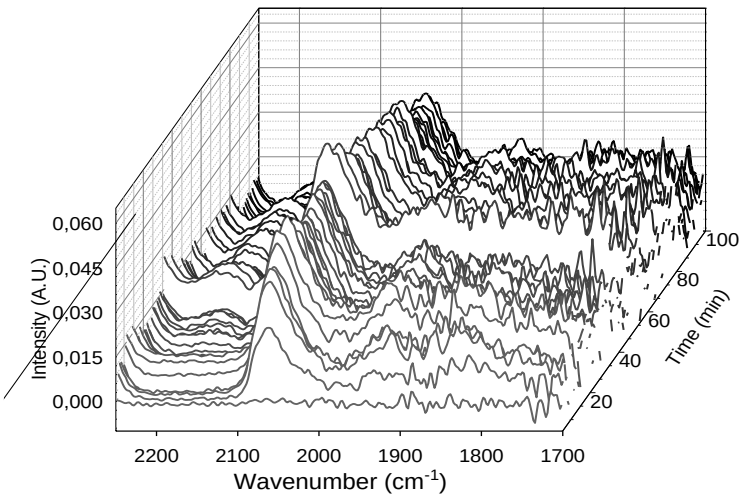

Figure 26 Operando FT-IR spectra of NiNP1.4@SiO_2Mw sample (A) during the CO_2 hydrogenation experiment (temperature 200- 400 °C, ramp: 5 °C/min, H_2/CO_2 flow: 16/4 ml/min) between 1700-2250 cm^{-1} for the CO stretching vibrations.

formate species were excluded from the discussion of this study since formate bands appear below 1700 cm^{-1}.

In Figure 27, the important intermediates of the carbide pathway in all samples are visible. At 215 °C, no methane was formed, but the reaction intermediates were immediately detected after starting the gas flows. At 400 °C, the methane band appeared in the beginning, while the gaseous CO band showed a decrease (negative absorbance). At the end of 400 °C, the methane band was increased. However, a clear comparison between the samples could not be made using Figure 27 because of the shifts of baselines. In order to relate the difference in particle sizes to intermediates, the area of these four regions was integrated, and activities were calculated with the same calculations performed for methane and plotted versus time (Figure 28 left). The region between 1700-1980 cm^{-1} was attributed to CO_{ads} (bridged) and the region between 1980-2100 cm^{-1} was attributed to CO_{ads} (on top). For gaseous CO, the region between 2150-2230 cm^{-1} was integrated. For methane, the region between 3007-3027 cm^{-1} was chosen. After integrating the regions, the results were normalized between 0 and 1, with 1 corresponding to the maximum point (Figure 28right).

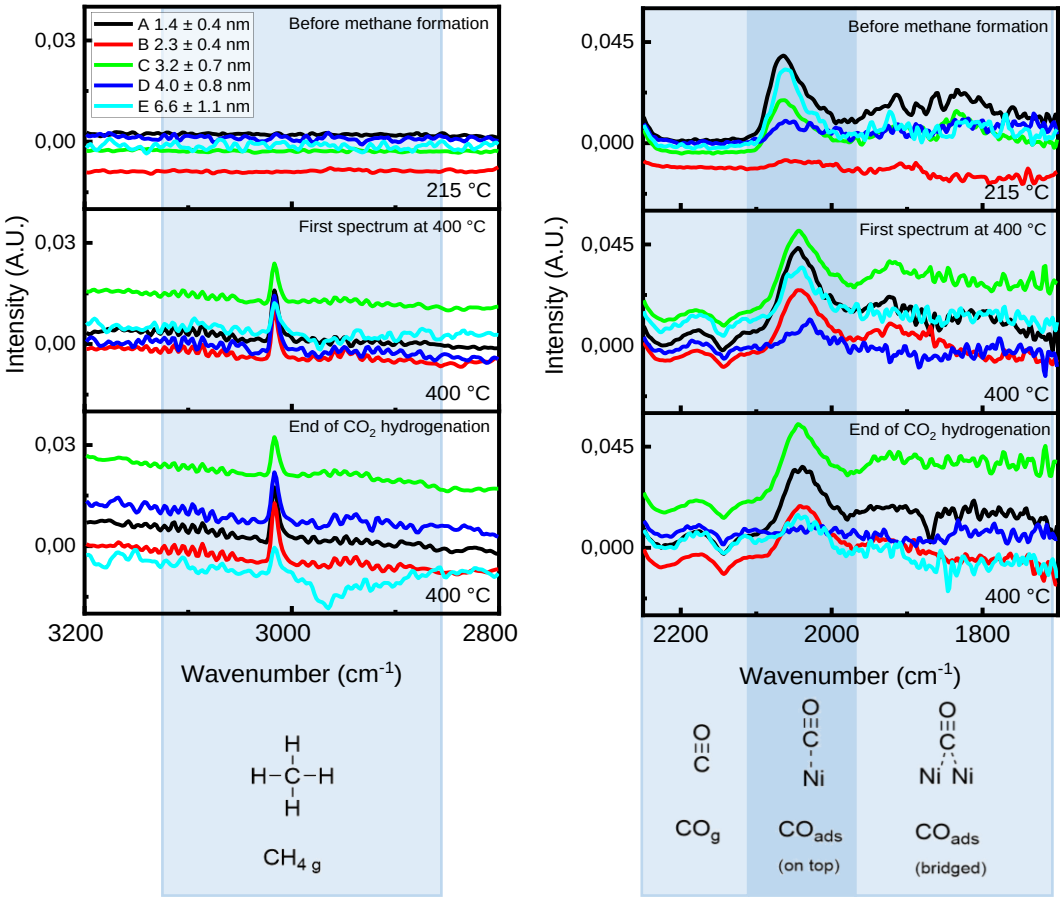

Figure 27 Operando FT-IR spectra of the samples A-E before, after start and at the end of CO_2 hydrogenation experiments (temperature 200-400 °C, ramp: 5 °C/min, H_2/CO_2 flow: 16/4 ml/min), focussed on methane, CO (g), CO_{ads} (top) and CO_{ads} (bridged) intermediates.

The CO_{ads} (bridged) curves were observed to lack a clear trend and exhibited a high degree of noise compared to the curves of other species. As a result, drawing conclusions from these CO_{ads} (bridged) curves was unreliable. Consequently, the CO_{ads} (bridged) curves were excluded from Figure 28 but are presented in Supplementary Information 8 (Figure SI 9).

On the other hand, at the beginning of the experiments, a sharp rise in the concentration of absorbed CO on a single Ni atom was seen. The CO_{ads} (top) amount decreases after reaching its

maximum, which is also the start of methane formation. The gaseous CO and methane curves start to increase after approximately 25 minutes. First, CO_2 was dissociated to CO (a sharp increase of red curves) after interaction with Ni atoms (CO_{ads}) and then to C on the Ni surface. This dissociation was followed by hydrogenation of the C atoms until stable CH4 (g) was formed. However, FT-IR was not suitable for detecting C*.

In all five samples, a clear decreasing trend is visible in the CO_{ads} (top) curve approximately after 25 minutes at 400 °C. The decrease is sharper in the curves of samples D and E in both non-normalized and normalized plots. The curves of samples A-C show a less sharp decrease. The substantial decrease in samples D and E explains the high activity results in Figure 24b. As explained in the activity part, the higher activity observed in samples D and E may be attributed to the choice of ligand and type of available facets in the samples. Additionally, fewer COads (top) intermediates on the surface could have resulted in less blockage, thereby providing more space for methane formation. It has been suggested that the larger Ni NPs may follow an H-assisted pathway, leading to increased activity.[21] However, these obtained data do not allow for a clear and reliable argument regarding the higher activity of larger Ni NPs (6.6 nm) than the activity of optimum Ni NP size (2.5 nm), as reported in Sterk et al. and Vogt et al.[1,2,21]

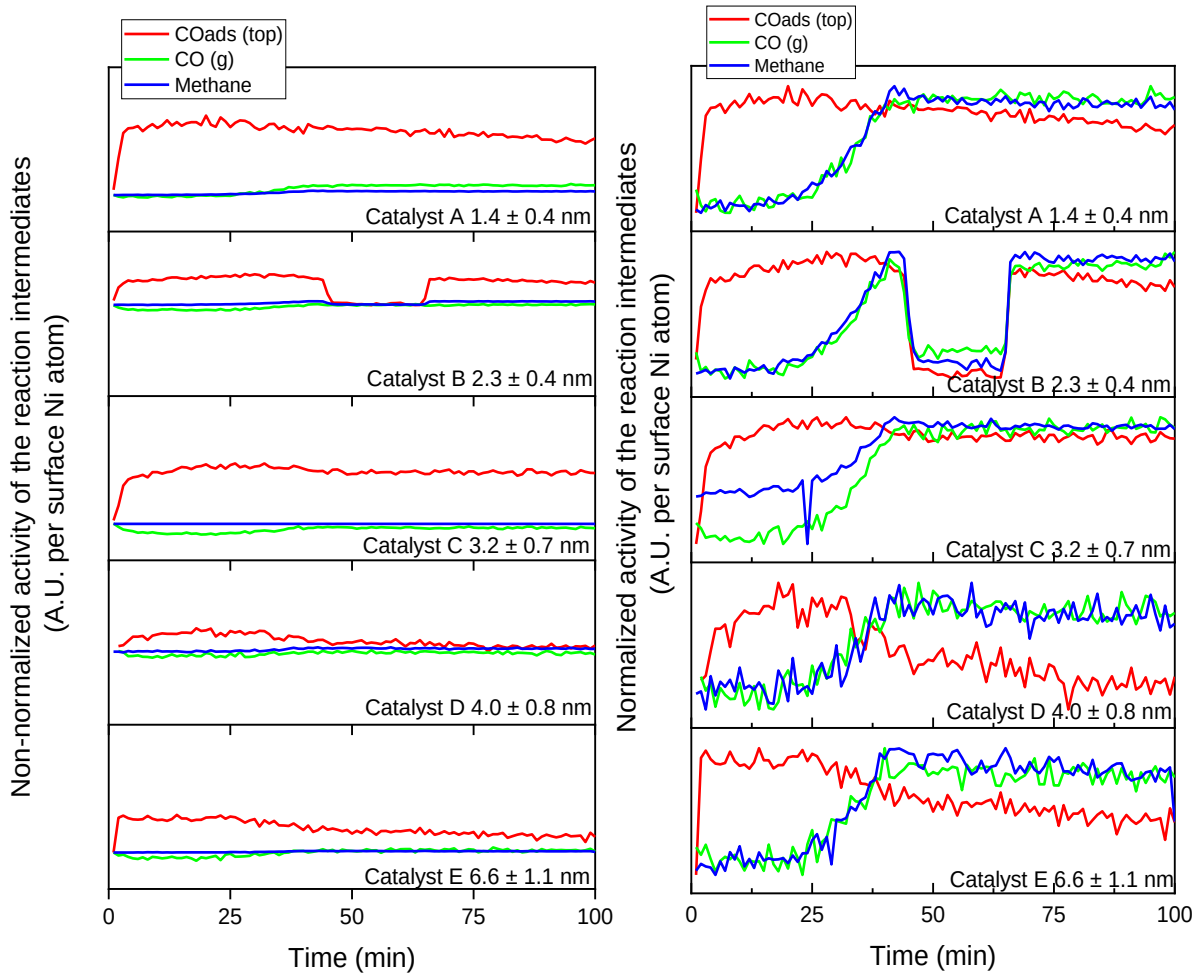

Figure 28 Calculated activity in A.U per surface Ni atom of the integrated FT-IR peak areas of CO (g), CO_{ads} (top) and methane bands plotted versus time with non-normalized (left) and normalized (right) plots. Normalization was done between 0 and 1 with 1 corresponding to the maximum calculated point in the non-normalized plot of each species. Experiment conditions: temperature: 200-400 °C, ramp: 5 °C/min, H_2/CO_2 flow: 16/4 ml/min.

Furthermore, it was discussed in the literature that the shift of CO_{ads} (top) peak upon temperature increase was due to the destabilization of carbonyl species and coverage effects. The coverage effect refers to the changes in the intensity and position of the IR bands due to the adsorption and coverage of reaction species (e.g. CO_2 and H_2) on the catalyst surface. For example, Terreni *et al.*[31] reported that CO_{ads} (top) peak appeared at 2045 cm^{-1} below 300 °C. The peak shifts to 2033 cm^{-1} when the temperature is 400 °C. Several studies have shown similar shifts of CO_{ads} (top) peak.[21,32] Figure 29 shows the CO_{ads} (top) peak heatmaps of CO_2 hydrogenation experiments of samples A-E. The CO_{ads} (top) peak was shifted during the experiments when the temperature was increased. The peak mostly appeared around 2060 cm^{-1} at 225 °C and shifted to around 2040 cm^{-1} at 400 °C. An exception is sample D, whereby the peak shifts from 2045 cm^{-1} to 2027 cm^{-1}. Nevertheless, a relation of Ni nanoparticle size with the peak shift could not be attributed to sample D.

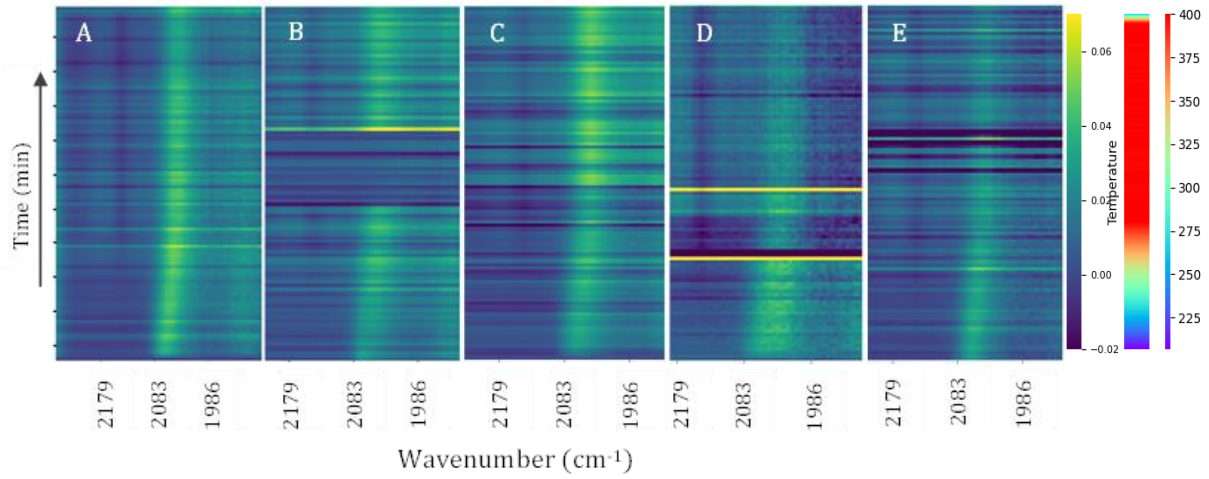

Figure 29 Heatmap of the CO_{ads} (top) peak during the CO_2 hydrogenation experiments of samples A-E. The peak shift from 2060 cm^{-1} to 2040 cm^{-1} approximately, except sample D (from 2045 cm^{-1} to 2027 cm^{-1}). Experiment conditions: temperature 200-400 °C, ramp: 5 °C/min, H_2/CO_2 flow: 16/4 ml/min.

In conclusion, the important intermediates of the carbide pathway could be identified and the activity of colloidal Ni catalysts with different nanoparticle sizes was calculated using operando FT-IR spectroscopy. To explore the reaction mechanism further, the SSITKA[52] technique and Raman spectroscopy can be used in the future. The activities of the samples were compared with a commercially available Ni catalyst, where the activities of the colloidal Ni catalyst were higher than the commercial Ni catalyst. It was also confirmed that ligands and ethyl groups were not participating in the CO_2 hydrogenation catalysis over colloidal Ni catalysts. This was confirmed when methane formation was stopped after turning off the CO_2 flow for 20 minutes during the CO_2 hydrogenation reaction. Interestingly, a characteristic activity trend could not be obtained, as reported by Sterk *et al.*[2] and Vogt *et al.*[1,21] The variation in activity may be due to the assumption that particle growth of supported Ni NPs at high temperatures did not occur, resulting in a new and distinct activity trend for silica-supported colloidal Ni NPs. With the assumption that was made, a new and different activity trend was shown for silica-supported colloidal Ni NPs, which requires more data to understand the effect of Ni nanoparticle size on the catalytic activity.

5. Conclusion

During this study, colloidal Ni nanoparticles were synthesized with various particle sizes. The particle sizes were tuned by varying reaction temperature (rt-90°C), reactant ratios and ligands (benzonitrile, mesitylamine and 4-tert-butylbenzonitrile). Colloidal Ni NPs with nanoparticle sizes from 1.4 nm to 6.6 nm were obtained, which were smaller than Ni NPs (3-4 nm) reported in Metin *et al.*[24] and Vrijburg *et al.*[10] Subsequently, the prepared colloidal Ni NPs were deposited on silica support to use in CO_2 hydrogenation catalysis experiments. After that, the ligands were removed using Meerwein's reagent, which also alkylated the silica surface. These alkyl groups were removed during the reduction experiments before the CO_2 hydrogenation experiments.

Five samples with an increasing nanoparticle size from 1.4 to 6.6 nm were tested for their catalytic activity during CO_2 hydrogenation experiments. The catalytic activity experiments showed that all samples were active during the methane formation. However, a characteristic maximum activity point around 2.5 nm Ni nanoparticle size was not observed during activity experiments. A clear argument for the obtained activity trend could not be given with obtained data. More data is needed to draw reliable conclusions about the probable causes. While particle size was the focus of this study, it is important to note that particle shape also has an important role in structure sensitivity reactions. As reported in Sterk *et al.*[2] the active sites are often stepped facets and found at the edges of Ni nanoparticles, likely because of the greater space they have for the adsorption of CO species. The particle shape of Ni NPs may have caused the different catalytic activities of the samples. For example, using different ligands in the synthesis of colloidal Ni NPs (sample E) could have affected the particle shape, leading to variations in catalytic activity.

In addition, it was confirmed that ethyl groups on the silica surface were not participating in the CO_2 hydrogenation experiments. Also, colloidal Ni catalysts showed higher activity compared to a commercial Ni catalyst, likely due to fewer defect sites in the colloidal Ni NPs.

Furthermore, the synthesis method for colloidal Ni nanoparticles was also applied to synthesize various colloidal metal nanoparticles. Hereby, colloidal Mn (3.4 nm), Fe (6.8 nm), Co (2.0 nm), Cu (1.4 nm) and Ru (8.1 nm) nanoparticles were successfully synthesized and the versatility of the synthesis method was confirmed.

6. Outlook

For the future of this research, calculating the catalytic activity in TOF values is crucial to compare them properly with the data from the literature. TOF calculations need GC, TEM and ICP data. The particle sizes of the spent samples should be determined using high-resolution TEM. GC is needed to determine the amount of methane gas. ICP is required to determine the Ni weight loading more accurately than AAS. Using *in-situ* XRD for CO_2 hydrogenation measurements could be a suitable technique to follow the changes in the sample during the CO_2 hydrogenation reaction. Additionally, the stability of the Ni NPs could be studied, which is an important issue in the industry. The sintering of Ni NPs at high temperatures is a well-known phenomenon.[22] Therefore, it is not unexpected that particle growth may have occurred during the performed catalytic activity measurements, leading to potential variations in the reported activity trend. To prevent particle growth, the Ni NPs can be protected by partially embedding the NPs into the silica matrix (Raspberry template), as described in van der Hoeven *et al.*[53]

The sample series could be expanded by preparing samples using the same ligands and larger Ni NPs (8-10 nm) to determine the effect of larger Ni NPs on catalytic activity. Besides, the effect of ligand removal on the activity could be evaluated more accurately.

The support effects on the activity of colloidal Ni NPs were not studied in this research. It is known that the supports can change the structure sensitivity, so the activity of nickel-based catalysts, as described in the Particle size effects section. Additionally, selectivity can also be affected by support, as described by Visser *et al.*[28] Thus, the research could focus on activity experiments using colloidal Ni NPs supported on different supports, such as graphitic carbon, titania, zirconia and ceria. The type of support could positively affect the removal of the ligands. For example, the study of Rosen *et al.*[49] reported very low IR absorbance for the ethyl groups on the titania surface after Meerwein's treatment, while the absorbance of ethyl groups on the ZnO surface was very strong. Studying the mechanism of the CO_2 hydrogenation reaction over various support is also essential. The structure sensitivity of Ni NPs smaller than 5 nm on other supports is not explored deeply as Ni NPs on the silica support. Also, the Ni loading of the catalyst could be increased. Higher Ni loading of the catalyst will be advantageous when XRD or XAS measurements going to be performed.

In the case of synthesizing other colloidal metal nanoparticles than Ni NP, selecting a precursor with a 2+ oxidation state instead of 3+ (Ru^{3+} and Fe^{3+}) could yield more monodisperse and smaller metal nanoparticles when BTB is used as a reducing agent because metal precursors with a 2+ oxidation state could be reduced faster. On the other hand, a more potent reducing agent could also be used to decrease the reducing agent effects.

With this synthesis method in hand, this work makes a valuable contribution to exploring the possible methods of CO_2 conversion to methane over nickel-based catalysts. The developed synthesis method will accelerate the research about nickel-based catalysts because the colloidal Ni NPs could be applied separately on different supports simultaneously. Additionally, the high ability to control the particle size will positively impact the efficiency of CO_2 conversion. It will result in a more efficient approach towards solving the climate change problem.

7. References

(1) Vogt, C.; Meirer, F.; Monai, M.; Groeneveld, E.; Ferri, D.; van Santen, R. A.; Nachtegaal, M.; Unocic, R. R.; Frenkel, A. I.; Weckhuysen, B. M. Dynamic Restructuring of Supported Metal Nanoparticles and Its Implications for Structure Insensitive Catalysis. *Nat. Commun.* **2021**, *12*, 7096.

(2) Sterk, E. B.; Nieuwelink, A. E.; Monai, M.; Louwen, J. N.; Vogt, E. T. C.; Filot, I. A. W.; Weckhuysen, B. M. Structure Sensitivity of CO_2 Conversion over Nickel Metal Nanoparticles Explained by Micro-Kinetics Simulations. *J. Am. Chem. Soc.* **2022**, *2*, 2714–2730.

(3) Vijayavenkataraman, S.; Iniyan, S.; Goic, R. A Review of Climate Change, Mitigation and Adaptation. *Renew. Sustain. Energy Rev.* **2012**, *16*, 878–897.

(4) Fawzy, S.; Osman, A. I.; Doran, J.; Rooney, D. W. Strategies for Mitigation of Climate Change: A Review. *Environ. Chem. Lett.* **2020**, *18*, 2069–2094.

(5) Ricke, K. L.; Millar, R. J.; MacMartin, D. G. Constraints on Global Temperature Target Overshoot. *Sci. Rep.* **2017**, *7*, 14743.

(6) Li, W.; Wang, H.; Jiang, X.; Zhu, J.; Liu, Z.; Guo, X.; Song, C. A Short Review of Recent Advances in CO_2 Hydrogenation to Hydrocarbons over Heterogeneous Catalysts. *RSC Adv.* **2018**, *8*, 7651–7669.

(7) Li, K.; Peng, B.; Peng, T. Recent Advances in Heterogeneous Photocatalytic CO_2 Conversion to Solar Fuels. *ACS Catal.* **2016**, *6*, 7485–7527.

(8) Yoon, Y.; Shoji Hall, A.; Surendranath, Y.; Yoon, Y.; Hall, A. S.; Surendranath, Y. Tuning of Silver Catalyst Mesostructure Promotes Selective Carbon Dioxide Conversion into Fuels. *Angew. Chemie Int. Ed.* **2016**, *55*, 15282–15286.

(9) Ye, R. P.; Ding, J.; Gong, W.; Argyle, M. D.; Zhong, Q.; Wang, Y.; Russell, C. K.; Xu, Z.; Russell, A. G.; Li, Q.; Fan, M.; Yao, Y. G. CO_2 Hydrogenation to High-Value Products via Heterogeneous Catalysis. *Nat. Commun.* **2019**, *10*, 5698.

(10) Vrijburg, W. L.; Van Helden, J. W. A.; Van Hoof, A. J. F.; Friedrich, H.; Groeneveld, E.; Pidko, E. A.; Hensen, E. J. M. Tunable Colloidal Ni Nanoparticles Confined and Redistributed in Mesoporous Silica for CO_2 Methanation. *Catal. Sci. Technol.* **2019**, *9*, 2578–2591.

(11) Liang, C.; Tian, H.; Gao, G.; Zhang, S.; Liu, Q.; Dong, D.; Hu, X. Methanation of CO_2 over Alumina Supported Nickel or Cobalt Catalysts: Effects of the Coordination between Metal and Support on Formation of the Reaction Intermediates. *Int. J. Hydrogen Energy* **2020**, *45*, 531–543.

(12) Kwak, J. H.; Kovarik, L.; Szanyi, J. CO_2 Reduction on Supported Ru/Al_2O_3 Catalysts: Cluster Size Dependence of Product Selectivity. *ACS Catal.* **2013**, *3*, 2449–2455.

(13) Karelovic, A.; Ruiz, P. Mechanistic Study of Low Temperature CO_2 Methanation over Rh/TiO_2 Catalysts. *J. Catal.* **2013**, *301*, 141–153.

(14) Park, J. N.; McFarland, E. W. A Highly Dispersed Pd–Mg/SiO_2 Catalyst Active for Methanation of CO_2. *J. Catal.* **2009**, *266*, 92–97.

(15) Murthy, P. S.; Liang, W.; Jiang, Y.; Huang, J. Cu-Based Nanocatalysts for CO_2 Hydrogenation to Methanol. *Energy and Fuels* **2021**, *35*, 8558–8584.

(16) Carvalho, D. F.; Almeida, G. C.; Monteiro, R. S.; Mota, C. J. A. Hydrogenation of CO_2 to Methanol and Dimethyl Ether over a Bifunctional Cu·ZnO Catalyst Impregnated on Modified γ-Alumina. *Energy and Fuels* **2020**, *34*, 7269–7274.

(17) Guo, L.; Sun, J.; Ji, X.; Wei, J.; Wen, Z.; Yao, R.; Xu, H.; Ge, Q. Directly Converting Carbon Dioxide to Linear α-Olefins on Bio-Promoted Catalysts. *Commun. Chem.* **2018**, *1*, 11.

(18) Chen, Y.; Peng, D. L.; Lin, D.; Luo, X. Preparation and Magnetic Properties of Nickel Nanoparticles via the Thermal Decomposition of Nickel Organometallic Precursor in Alkylamines. *Nanotechnology* **2007**, *18*, 505703.

(19) Li, Y.; Wen, J.; Ali, A. M.; Duan, M.; Zhu, W.; Zhang, H.; Chen, C.; Li, Y. Size Structure–Catalytic Performance Correlation of Supported Ni/MCF-17 Catalysts for CO_x-Free Hydrogen Production. *Chem. Commun.* **2018**, *54*, 6364–6367.

(20) Senderens, J. B.; Sabatier, P. Nouvelles Synthèses Du Méthane. *Comptes Rendus* **1902**, *82*, 514–516.

(21) Vogt, C.; Groeneveld, E.; Kamsma, G.; Nachtegaal, M.; Lu, L.; Kiely, C. J.; Berben, P. H.; Meirer, F.; Weckhuysen, B. M. Unravelling Structure Sensitivity in CO_2 Hydrogenation over Nickel. *Nat. Catal.* **2018**, *1*, 127–134.

(22) Rinaldi, R.; Porcari, A. de M.; Rocha, T. C. R.; Cassinelli, W. H.; Ribeiro, R. U.; Bueno, J. M. C.; Zanchet, D. Construction of Heterogeneous Ni Catalysts from Supports and Colloidal Nanoparticles - A Challenging Puzzle. *J. Mol. Catal. A Chem.* **2009**, *301*, 11–17.

(23) Zacharaki, E.; Beato, P.; Tiruvalam, R. R.; Andersson, K. J.; Fjellvåg, H.; Sjåstad, A. O. From Colloidal Monodisperse Nickel Nanoparticles to Well-Defined Ni/Al_2O_3 Model Catalysts. *Langmuir* **2017**, *33*, 9836–9843.

(24) Metin, Ö.; Özkar, S.; Sun, S. Monodisperse Nickel Nanoparticles Supported on SiO_2 as an Effective Catalyst for the Hydrolysis of Ammonia-Borane. *Nano Res.* **2010**, *3*, 676–684.

(25) Tao, F.; Dag, S.; Wang, L. W.; Liu, Z.; Butcher, D. R.; Bluhm, H.; Salmeron, M.; Somorjai, G. A. Break-up of Stepped Platinum Catalyst Surfaces by High CO Coverage. *Science* **2010**, *327*, 850–853.

(26) Van Bokhoven, J. A.; Miller, J. T. D Electron Density and Reactivity of the d Band as a Function of Particle Size in Supported Gold Catalysts. *J. Phys. Chem. C* **2007**, *111*, 9245–9249.

(27) Van Santen, R. A. Complementary Structure Sensitive and Insensitive Catalytic Relationships. *Acc. Chem. Res.* **2009**, *42*, 57–66.

(28) Visser, N. L.; Daoura, O.; Plessow, P. N.; Smulders, L. C. J.; de Rijk, J. W.; Stewart, J. A.; Vandegehuchte, B. D.; Studt, F.; van der Hoeven, J. E. S.; de Jongh, P. E. Particle Size Effects of Carbon Supported Nickel Nanoparticles for High Pressure CO_2 Methanation. *ChemCatChem* **2022**, *14*, e2022006.

(29) Sabatier, P.; Senderens, J. B. Hydrogénation Directe Des Oxydes Du Carbone En Présence de Divers Métaux Divisés. *Comptes Rendus* **1903**, *134*, 689–691.

(30) Vogt, C.; Kranenborg, J.; Monai, M.; Weckhuysen, B. M. Structure Sensitivity in Steam and Dry Methane Reforming over Nickel: Activity and Carbon Formation. *ACS Catal.* **2020**, *10*, 1428–1438.

(31) Terreni, J.; Sambalova, O.; Borgschulte, A.; Rudić, S.; Parker, S. F.; Ramirez-Cuesta, A. J. Volatile Hydrogen Intermediates of CO_2 Methanation by Inelastic Neutron Scattering. *Catalysts* **2020**, *10*, 433.

(32) Zarfl, J.; Ferri, D.; Schildhauer, T. J.; Wambach, J.; Wokaun, A. DRIFTS Study of a Commercial $Ni/\gamma\text{-}Al_2O_3$ CO Methanation Catalyst. *Appl. Catal. A Gen.* **2015**, *495*, 104–114.

(33) Khan, M. D.; Opallo, M.; Revaprasadu, N. Colloidal Synthesis of Metal Chalcogenide

Nanomaterials from Metal–Organic Precursors and Capping Ligand Effect on Electrocatalytic Performance: Progress, Challenges and Future Perspectives. *Dalt. Trans.* **2021**, *50*, 11347–11359.

(34) Hyeon, T. Chemical Synthesis of Magnetic Nanoparticles. *Chem. Commun.* **2003**, *3*, 927–934.

(35) Murray, C. B.; Norris, D. J.; Bawendi, M. G. Synthesis and Characterization of Nearly Monodisperse CdE (E = S, Se, Te) Semiconductor Nanocrystallites. *J. Am. Chem. Soc.* **1993**, *115*, 8706–8715.

(36) Gibbs, J. W. On the Equilibrium of Heterogeneous Substances. *Trans. Connect. Acad.* **1876**, *3*, 108.

(37) Xia, Y.; Gilroy, K. D.; Peng, H. C.; Xia, X. Seed-Mediated Growth of Colloidal Metal Nanocrystals. *Angew. Chemie Int. Ed.* **2017**, *56*, 60–95.

(38) Wang, Y.; He, J.; Liu, C.; Chong, W. H.; Chen, H. Thermodynamics versus Kinetics in Nanosynthesis. *Angew. Chemie Int. Ed.* **2015**, *54*, 2022–2051.

(39) Groeneveld, E.; De Mello Donegá, C. The Challenge of Colloidal Nanoparticle Synthesis. In *Nanoparticles: Workhorses of Nanoscience*; Springer-Verlag Berlin Heidelberg, 2014; pp 145–189.

(40) Yin, Y.; Alivisatos, A. P. Colloidal Nanocrystal Synthesis and the Organic–Inorganic Interface. *Nature* **2005**, *437*, 664–670.

(41) Heuer-Jungemann, A.; Feliu, N.; Bakaimi, I.; Hamaly, M.; Alkilany, A.; Chakraborty, I.; Masood, A.; Casula, M. F.; Kostopoulou, A.; Oh, E.; Susumu, K.; Stewart, M. H.; Medintz, I. L.; Stratakis, E.; Parak, W. J.; Kanaras, A. G. The Role of Ligands in the Chemical Synthesis and Applications of Inorganic Nanoparticles. *Chem. Rev.* **2019**, *119*, 4819–4880.

(42) Yang, T. H.; Shi, Y.; Janssen, A.; Xia, Y. Surface Capping Agents and Their Roles in Shape-Controlled Synthesis of Colloidal Metal Nanocrystals. *Angew. Chemie Int. Ed.* **2020**, *59*, 15378–15401.

(43) Pradhan, N.; Reifsnyder, D.; Xie, R.; Aldana, J.; Peng, X. Surface Ligand Dynamics in Growth of Nanocrystals. *J. Am. Chem. Soc.* **2007**, *129*, 9500–9509.

(44) Yoskamtorn, T.; Yamazoe, S.; Takahata, R.; Nishigaki, J. I.; Thivasasith, A.; Limtrakul, J.; Tsukuda, T. Thiolate-Mediated Selectivity Control in Aerobic Alcohol Oxidation by Porous Carbon-Supported Au_{25} Clusters. *ACS Catal.* **2014**, *4*, 3696–3700.

(45) Moreno, M.; Ibañez, F. J.; Jasinski, J. B.; Zamborini, F. P. Hydrogen Reactivity of Palladium Nanoparticles Coated with Mixed Monolayers of Alkyl Thiols and Alkyl Amines for Sensing and Catalysis Applications. *J. Am. Chem. Soc.* **2011**, *133*, 4389–4397.

(46) Rossi, L. M.; Fiorio, J. L.; Garcia, M. A. S.; Ferraz, C. P. The Role and Fate of Capping Ligands in Colloidally Prepared Metal Nanoparticle Catalysts. *Dalt. Trans.* **2018**, *47*, 5889–5915.

(47) Zhang, H. T.; Wu, G.; Chen, X. H.; Qiu, X. G. Synthesis and Magnetic Properties of Nickel Nanocrystals. *Mater. Res. Bull.* **2006**, *41*, 495–501.

(48) Carenco, S.; Boissière, C.; Nicole, L.; Sanchez, C.; Le Floch, P.; Mézailles, N. Controlled Design of Size-Tunable Monodisperse Nickel Nanoparticles. *Chem. Mater.* **2010**, *22*, 1340–1349.

(49) Rosen, E. L.; Buonsanti, R.; Llordes, A.; Sawvel, A. M.; Milliron, D. J.; Helms, B. A. Exceptionally Mild Reactive Stripping of Native Ligands from Nanocrystal Surfaces by Using Meerwein's Salt. *Angew. Chemie Int. Ed.* **2012**, *51*, 684–689.

(50) Nelson, A.; Zong, Y.; Fritz, K. E.; Suntivich, J.; Robinson, R. D. Assessment of Soft Ligand Removal Strategies: Alkylation as a Promising Alternative to High-Temperature Treatments for Colloidal Nanoparticle Surfaces. *ACS Mater. Lett.* **2019**, *1*, 177–184.

(51) Sahu, N.; Brahme, N.; Sharma, R. Effect of Capping Agent on the Particle Size of CdSe Nanoparticles. *Luminescence* **2016**, *31*, 1400–1406.

(52) Ledesma, C.; Yang, J.; Chen, D.; Holmen, A. Recent Approaches in Mechanistic and Kinetic Studies of Catalytic Reactions Using SSITKA Technique. *ACS Catal.* **2014**, *4*, 4527–4547.

(53) Van Der Hoeven, J. E. S.; Krämer, S.; Dussi, S.; Shirman, T.; Park, K.-C. K.; Rycroft, C. H.; Bell, D. C.; Friend, C. M.; Aizenberg, J. On the Origin of Sinter-Resistance and Catalyst Accessibility in Raspberry-Colloid-Templated Catalyst Design. *Adv. Funct. Mater.* **2021**, *31*, 2106876.

Abbreviations

NP	:	Nanoparticle
BTB	:	Borane tert-butylamine complex
DFT	:	Density functional theory
MKM	:	Micro-kinetics modelling
TOF	:	Turn-over frequency
OAm	:	Oleylamine
PhCN	:	Benzonitrile
MesNH	:	2,4,6-trimethylaniline, mesitylamine
4-TBBN	:	4-tert-butylbenzonitrile
Mw	:	Meerwein's reagent
TEM	:	Transmission Electron Microscopy
TPR	:	Temperature Programmed Reduction
AAS	:	Atomic Absorption Spectroscopy
IR	:	Infrared Spectroscopy
FT-IR	:	Fourier Transform Infrared Spectroscopy
TCD	:	Thermal Conductivity Detector
TEOS	:	Tetraethyl orthosilicate
HDP	:	Homogenous deposition precipitation

Supplementary Information

1. Washing step of the synthesis product

The washing with hexane resulted in TEM images with large needle-like shapes (Figure SI 1a). It was concluded that they were organic materials (waste) from the reaction after comparing them with the TEM image of the hexane waste (Figure SI 1b).

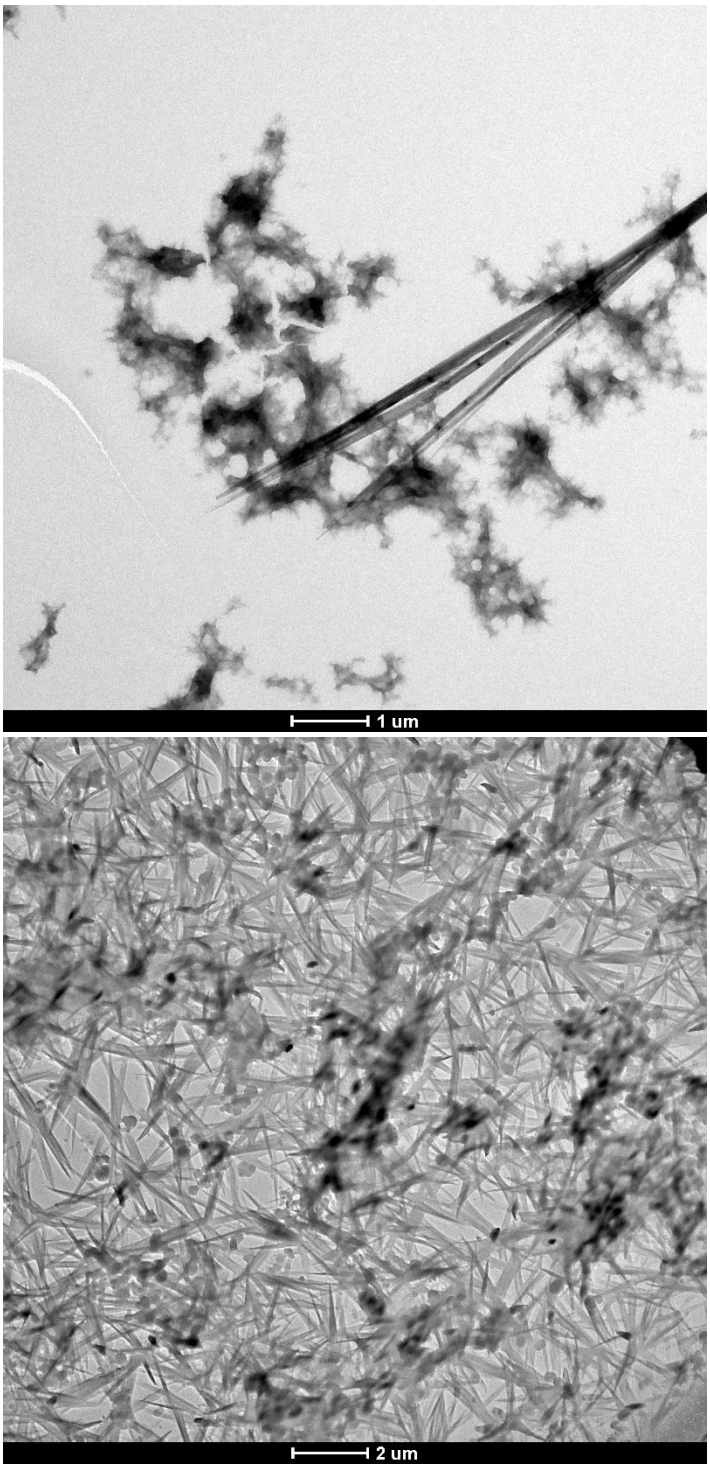

Figure SI 1 TEM images of batches during the selection of the washing method after the synthesis of 2.8 nm Ni NPs at 50 °C: a) large needles caused by organic waste from the reaction in the product batch, b) needles in the hexane waste from the reaction.

2. The overview of the syntheses

Table SI 1 gives an overview of performed syntheses. Seventeen different colloidal Ni NP syntheses were performed in total. Different metal precursors, ligands, reaction temperatures, and reactant ratios were chosen during the syntheses. Bram Kappé synthesised 2.0 nm Co NPs and 3.8 nm Ni NPs.

Table SI 1 An overview of the performed syntheses is given with the determined average particle size of counted particles (N). Bram Kappé performed syntheses BK008 and BK018.

SYNTHESIS	SAMPLE CODE	PRECURSOR	LIGAND	PARTICLE SIZE (NM)	ST. DEV. (NM)	ST. DEV. (%)	N
MS01	NiNP(PhCN)1.9	$Ni(acac)_2$	Benzonitrile	1.9	0.3	17.6	205
MS02	NiNP(PhCN)2.8	$Ni(acac)_2$	Benzonitrile	2.8	0.6	20.6	220
MS07	NiNP(PhCN)4.4	$Ni(acac)_2$	Benzonitrile	4.4	1.3	29.5	298
MS11	NiNP(PhCN)1.5	$Ni(acac)_2$	Benzonitrile	1.5	0.4	22.9	471
MS12	NiNP(PhCN)1.6	$Ni(acac)_2$	Benzonitrile	1.6	0.4	21.7	392
MS14	NiNP(PhCN)1.4	$Ni(acac)_2$	Benzonitrile	1.4	0.4	29.7	213
MS15	NiNP(PhCN)2.8	$Ni(acac)_2$	4-tert-butylbenzonitrile	3.4	0.9	26.5	150
MS16	RuNP(MesNH)8.1	$Ru(acac)_3$	MesNH	8.1	1.4	17.0	220
MS18	NiNP(MesNH)6.1	$Ni(acac)_2$	MesNH	6.6	1.1	16.8	41
MS19	NiNP(PhCN)4.0	$Ni(acac)_2$	Benzonitrile	4.0	0.8	21.0	104
MS24	NiNP(PhCN)2.5	$Ni(acac)_2$	Benzonitrile	2.5	0.4	16.0	108
MS25	FeNP(MesNH)6.8	$Fe(acac)_3$	MesNH	6.8	1.6	23.5	101
MS26	MnNP(MesNH 3.4	$Mn(acac)_2$	MesNH	3.4	0.6	17.6	118
MS27	CuNP(MesNH)1.4	$Cu(acac)_2$	MesNH	1.4	0.3	21.4	69
MS28	NiNP(PhCN)2.3	$Ni(acac)_2$	Benzonitrile	2.3	0.4	17.0	117
MS29	NiNP(PhCN)2.8	$Ni(acac)_2$	Benzonitrile	2.8	0.6	21.4	119
MS30	NiNP(PhCN)3.2	$Ni(acac)_2$	Benzonitrile	3.2	0.7	21.9	107
BK008	NiNP(MesNH)3.8	$Ni(acac)_2$	MesNH	3.8	0.5	13.7	93
BK018	CoNP(MesNH)2.0	$Co(acac)_2$	MesNH	2.0	0.4	19.5	134

3. TEM images of colloidal Ni NPs after the syntheses with different reactant ratios

Figure SI 2 and Figure SI 3 give the TEM images of colloidal Ni NPs after the syntheses with different reactant ratios.

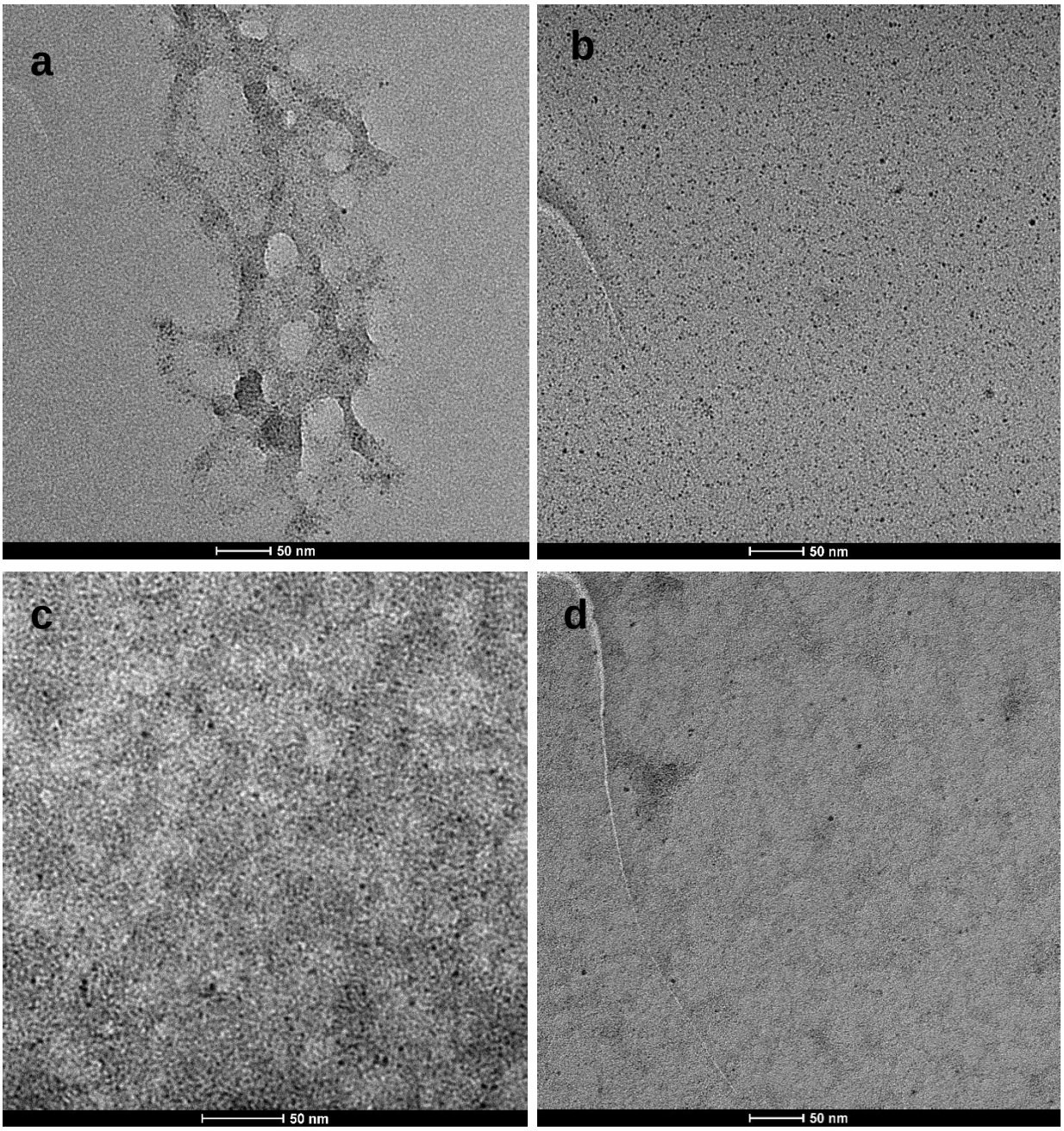

Figure SI 2 TEM images of colloidal Ni NPs after the syntheses with different reactant ratios: a) 1.4 ± 0.4 nm Ni NPs (Table 2, row 1), b) 1.6 ± 0.4 nm Ni NPs (Table 2, row 2), c) 2.1 ± 0.4 nm Ni NPs. (Table 2, row 3) and d) 3.2 ± 0.7 nm Ni NPs. (Table 2, row 4).

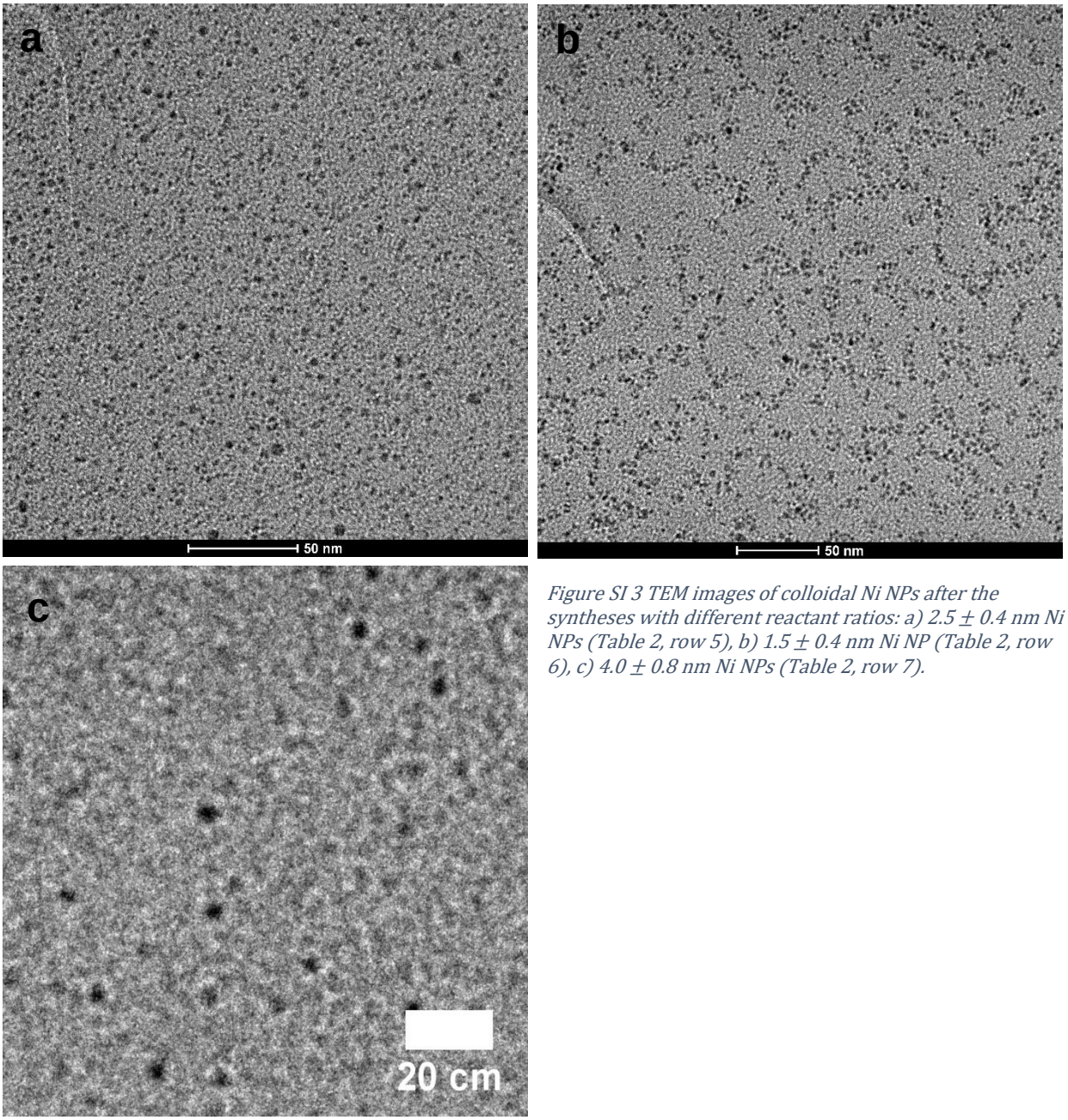

Figure SI 3 TEM images of colloidal Ni NPs after the syntheses with different reactant ratios: a) 2.5 ± 0.4 nm Ni NPs (Table 2, row 5), b) 1.5 ± 0.4 nm Ni NP (Table 2, row 6), c) 4.0 ± 0.8 nm Ni NPs (Table 2, row 7).

4. Calculation of Ni weight loading using AAS

Below are the formulae for Ni wt.% calculation with the raw data given.

$$Ni\ in\ the\ flask\ (mg) = concentration\left(\frac{mg}{L}\right) x\ \frac{dilution\ factor}{1000} \quad (1)$$

$$Ni\ wt.\% = \frac{mg\ Ni\ in\ flask\ (mg)}{sample\ weight\ (mg)} x\ 100\% \quad (2)$$

First, concentration (mg/L) is obtained from AAS results using the polynomial degree (Table SI 2), multiplied by the dilution factor and divided by factor 1000. Then, this yielded the amount of Ni in the volumetric flask (mg in Ni in the flask). After that, Ni in the flask (mg) is divided by the sample weight (mg) to get the Ni loading of the sample, which is then multiplied by 100 to get Ni wt.%.

Table SI 2 Raw data of AAS measurements for determining the samples' Ni weight loading (wt. %).

AAS01 data						
Cal-std (mg/L)		Abs				
1	0	0.00005				
2	10	0.16807				
3	20	0.2931				
4	30	0.40766				
5	40	0.4912	from polynomial degree: 2			
6	50	0.57645				
7	60	0.62894	Concentration (mg/l)	weight sample (mg)	Ni in flask (mg)	**Ni wt.%**
NiNP1.9@ SiO_2Mw	MS01	0.09738	5.813	60.4	0.29	**0.48**
NiNP4.4@ SiO_2Mw	MS09	0.02585	1.241	61.9	0.06	**0.10**
NiNP2.8@ SiO_2Mw	MS17	0.12863	7.898	61.7	0.39	**0.64**
NiNP4.0@ SiO_2Mw	MS22	0.17292	10.959	61.4	0.55	**0.89**

AAS02 data						
Cal-std	(mg/L)	Abs				
1	0	0.0023				
2	10	0.17675				
3	20	0.33179				
4	30	0.45401				
5	40	0.53463	from polynomial degree:			
6	50	0.6289	2			
7	60	0.69084	Concentration (mg/l)	weight sample (mg)	Ni in flask (mg)	**Ni wt.%**
NiNP1.4@ SiO_2Mw	MS031	0.27141	16.2930	64.2	0.41	**0.63**
NiNP2.3@ SiO_2Mw	MS032	0.26016	15.5180	61.1	0.39	**0.63**
NiNP3.2@ SiO_2Mw	MS033	0.30599	18.7360	59.4	0.47	**0.79**
NiNP4.0@ SiO_2Mw	MS46_1	0.36208	22.9210	127.8	1.15	**0.90**
NiNP(PhCN)4.0@SiO_2	MS46_2	0.48317	33.2100	122.0	0.83	**0.68**
NiNP6.6@ SiO_2Mw	MS47	0.35288	22.2140	66.5	0.56	**0.84**

5. *Extra performed techniques to remove the ethyl groups*

To remove the ligands, different concentrations (4, 8, 12.5 and 25%) of ammonia solution were used (Scheme SI 1).[1,2] The method was adapted from the work of Matsoukas *et al.*, where they had hydrolyzed tetraethyl orthosilicate (TEOS) with 30% NH_3 to synthesize colloidal Si particles.[3]

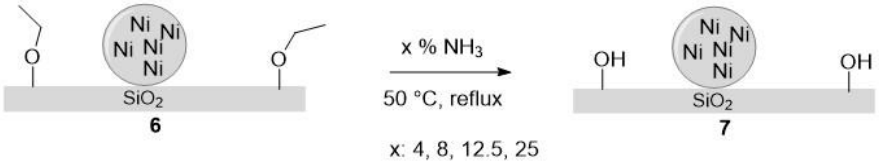

Scheme SI 1 Removal of ethyl groups from the SiO_2 surface using NH_3 solution.

Figure SI 4 shows the FT-IR spectra of the samples after the ammonia treatments. First, the samples NiNP4.4@SiO_2Mw and NiNP2.8@SiO_2Mw were refluxed with 4% and 8% NH_3 solution for 45 minutes while stirring. 4% and 8% NH_3 had decreased the intensity of the strong C-H band but was not removed completely. (Figure SI 4a, b). In both cases, the intensity of the OH band around 3700 cm^{-1} was clearly increased. Indicating the O-atoms on the SiO_2 surface were hydroxylated to form OH groups.

Subsequently, an 12.5% NH_3 solution was used to treat the NiNP4.0@SiO_2Mw sample. Here, the strong band of C-H stretching of ethyl groups was removed even in the first spectrum of the reduction experiment (Figure SI 4c). However, the removal of the ethyl groups using a 12.5 % NH_3 solution was not reproducible (Figure SI 4d, e). The samples were even treated with 25% NH_3 solution or treated twice with NH_3 solution (Figure SI 4f), but no considerable changes in the ethyl group intensity were visible.

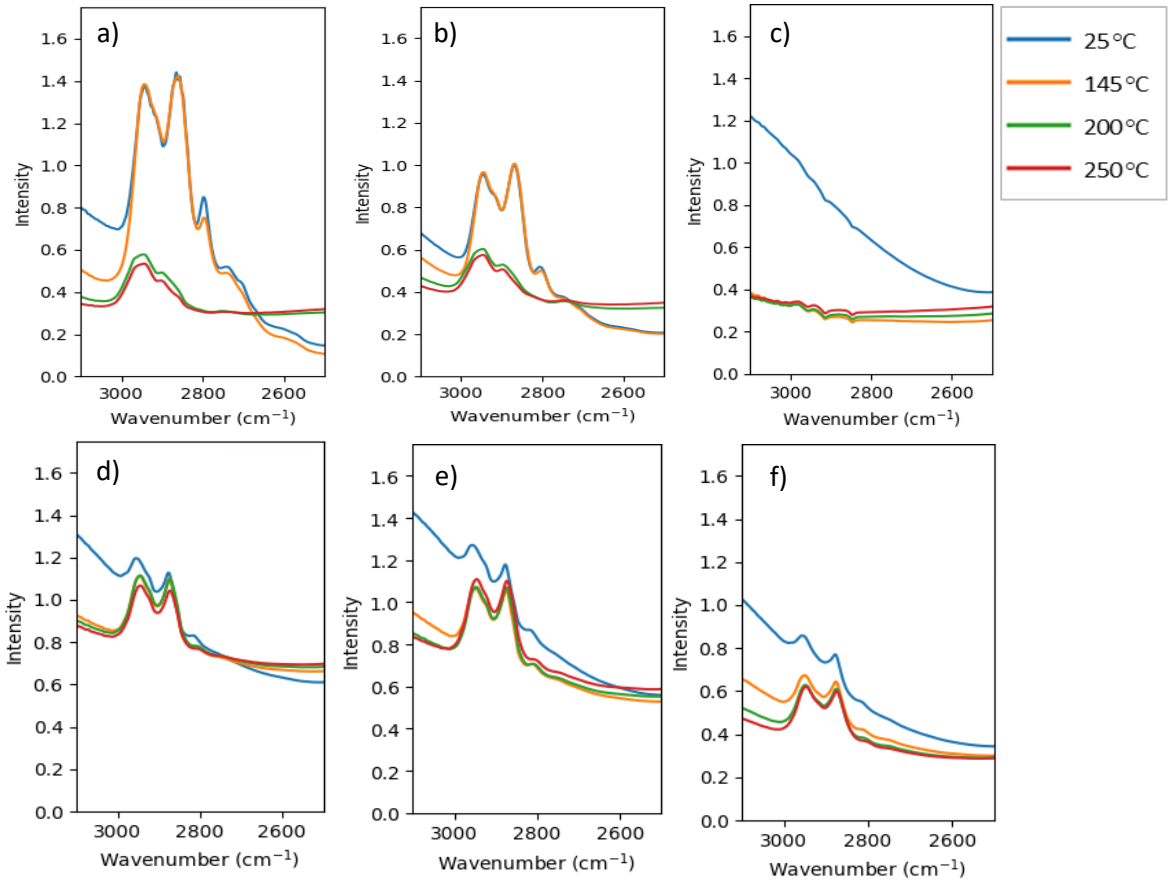

Figure SI 4 DRIFTS spectra of the samples during calcination and reduction experiments: NiNP4.4@SiO_2Mw4%NH_3 (a), NiNP2.8@SiO_2Mw8%NH_3 (b), NiNP4.0@SiO_2Mw12.5%NH_3 during reduction experiment (c), NiNP1.4@SiO_2Mw12.5%NH_3 (d), NiNP3.2@SiO_2Mw12.5%NH_3 (e), NiNP3.2@SiO_2Mw25%NH_3 (f).

Because the NH_3 treatments were performed on samples with different Ni nanoparticle sizes, a question was raised about the role of Ni nanoparticle sizes in the alkylation of the SiO_2 surface. Therefore, the alkylation of the SiO_2 surface with Meerwein's reagent was studied without deposition of the colloidal Ni NPs. The sample was prepared by treating the SiO_2 support first with Meerwein's reagent (Figure SI 5a), then with 12.5% NH_3 solution (Figure SI 5b) in the same way as supported Ni NPs.

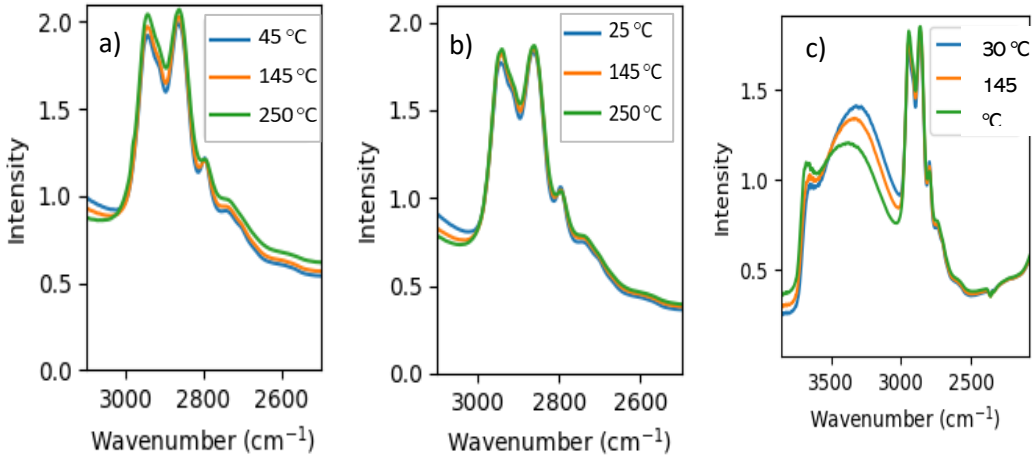

Figure SI 5 DRIFTS spectra of Meerwein's reagent treated @SiO_2Mw sample (a), Meerwein's reagent treated @SiO_2Mw12.5%NH_3 sample (b) and Meerwein's reagent treated @SiO_2Mw25%NH_3/methanol (c).

The spectra in Figure SI 5 show that Meerwein's reagent was alkylating the SiO_2 surface. The slight decrease in the absorbance in Figure SI 5b shows the partial removal of the ethyl groups after NH_3 treatment. More importantly, spectra confirm that Ni NPs had no role in the alkylation and removal step because the absorbance of the corresponding bands was comparable in the samples with Ni NPs. After that, to force the hydrolysis of the alkylated SiO_2 surface, methanol was added to the solution of 25% NH_3 (6:4 ml). This addition of methanol was reported by Malay *et al.* They obtained the highest hydrolysis rate of TEOS when a methanol/ammonia mixture was used.[3] But in our case, unfortunately, methanol addition did not result in better ethyl group removal, as seen in Figure SI 5c.

The ligand removal was also performed using Meerwein's reagent before the deposition on SiO_2 support to prevent the alkylation of the support surface. Meerwein's reagent was added to a vial with colloidal Ni NPs dissolved in toluene (1 ml). Chloroform was added after stirring the vial for 2 minutes, followed by removing the solvents. The product was washed once with chloroform. ATR-IR spectrum showed that the absorbance band of aromatic C-H stretching vibrations was still present in the sample. Therefore, this method was considered as not working. Also, the removal of the ligands was tried using 15% formic acid and 17% acetic acid with unsupported Ni NPs.[4] But using formic and acetic acids resulted in larger Ni NPs (Figure SI 6). Because of this, it was decided not to use these acids for ligand removal.

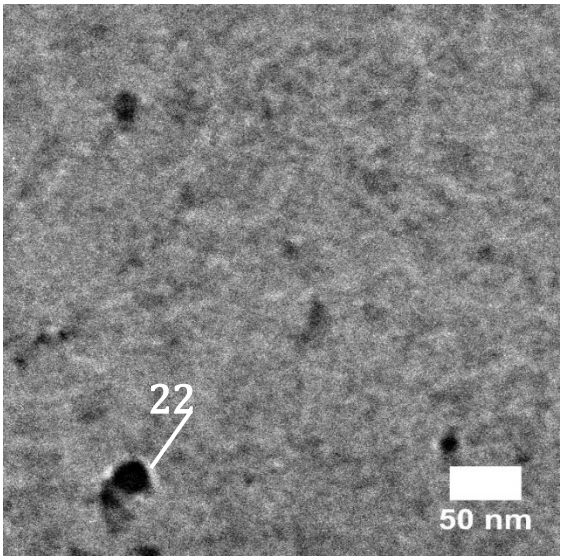

Figure SI 6 TEM image of the NiNP2.8(PhCN)after the treatment with formic acid. The particle size was grown from 2.8 nm to about 20 nm.

Method- Removal of the ethyl groups from silica-supported Ni NPs using NH_3
442 mg of Meerwein's reagent-treated Ni/SiO_2 was transferred to a two-necked round-bottomed flask, followed by adding 25 ml of 12.5% NH_3 to the two-necked flask. The solution was refluxed for at least 45 minutes at 50 °C while stirring. Then the solution was cooled to room temperature. The ammonia solution was removed, and the product was washed with water (2 times). Finally, the product was left in the oven overnight to dry, yielding a white powder (339mg, 76.6%).

6. The activity calculations

Below are catalytic activity calculations using the integrated methane peak given, as explained in section 0.

$$Amount\ of\ Ni = \frac{Weight\ of\ sample\ (mg)\ x\ Ni\ weight\ loading}{100} \quad (3)$$

$$Amount\ of\ Ni\ (g) = \frac{Amount\ of\ Ni}{1000} \quad (4)$$

$$Ni\ (mol) = \frac{\frac{Amount\ of\ Ni}{1000}}{58.6934\ u} \quad (5)$$

$$Volume\ of\ Ni = \frac{Amount\ of\ Ni}{890800\ g/cm^3} \quad (6)$$

$$Volume\ of\ one\ Ni\ NP = \frac{4}{3}\ x\ \pi\ x\ \left(\frac{Particle\ size}{2} x\ 10^{-9}\right)^3 \quad (7)$$

$$Amount\ of\ Ni\ NP = \frac{Volume\ of\ Ni}{Volume\ of\ one\ Ni\ NP} \quad (8)$$

$$Ni\ surface\ area = Amount\ of\ Ni\ NP\ x\ 4\ x\ \pi\ x\ \left(\frac{Particle\ size}{2} x\ 10^{-9}\right)^2 \quad (9)$$

$$Amount\ of\ Ni\ atoms\ on\ surface = (Ni\ surface\ area\ x\ 10^{18}) x\ 10 \quad (9)$$

$$Ni\ atoms\ on\ surface\ (mol) = \left(\frac{Amount\ of\ Ni\ atom\ surface}{6.0221409\ x\ 10^{23}}\right) \quad (10)$$

7. TEM image of the spent sample C

Figure SI 7 shows the spent sample C used in the catalytic activity experiments. The Ni NP were grown from 3.2 nm to 6.5 nm after the reduction and CO_2 hydrogenation experiments. They were detected separately from the silica support. Detection of the silica-supported Ni NPs was not possible.

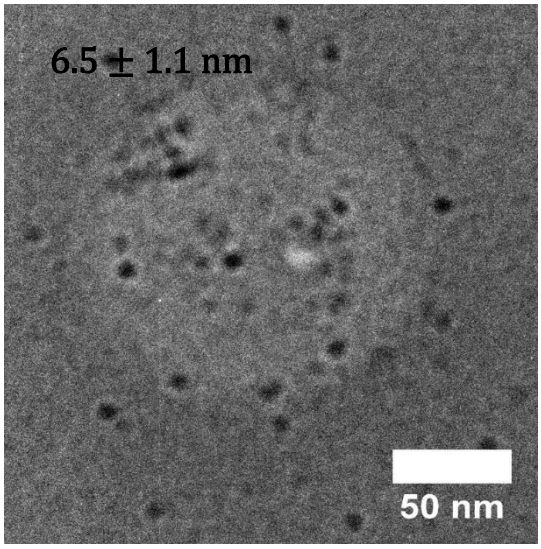

Figure SI 7 TEM image of the spent NiNP3.2@SiO_2Mw sample (C) with particle size of 6.5 ± 1.1 nm.

8. Catalytic activity plots

Figure SI 8 shows the uncorrected catalytic activity plots of samples A-E and H.

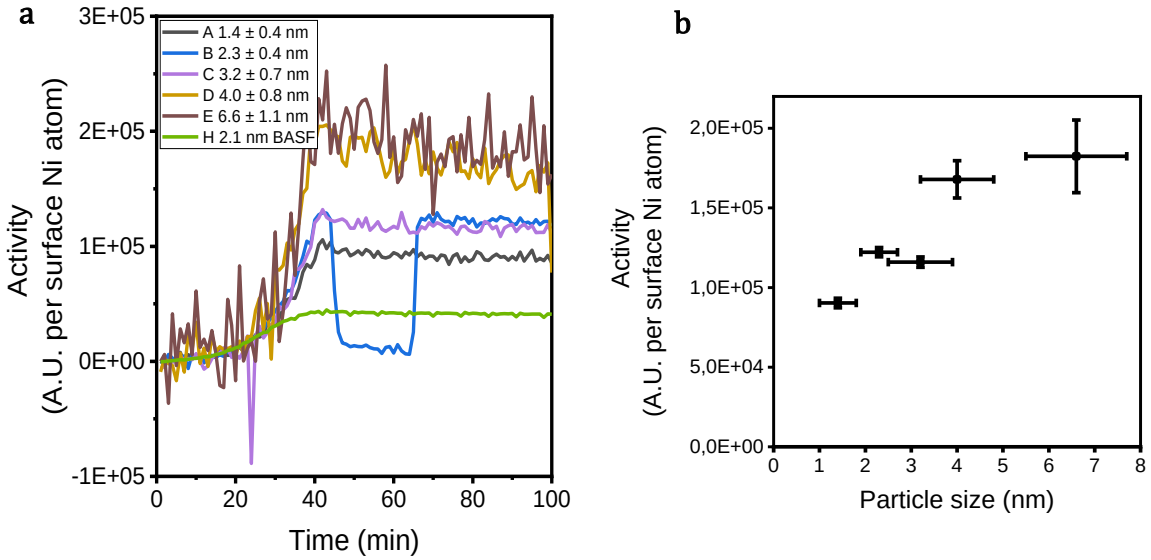

Figure SI 8 The activity of the samples A-E by integrating the methane peak (c) versus time and versus particle size (d).

In Figure SI 9, integrated FT-IR peak areas of CO (g), CO_{ads} (top), *CO_{ads} (bridged)* and methane are plotted versus time (normalized). In an ideal situation, as explained in Vogt *et al.*,[21] the CO_{ads} (bridged) intermediate will have a higher concentration at the beginning of the reaction. Then, it will decrease and reach a plateau until the experiment's end, while the COads (bridged) curves in Figure SI 9 do not follow the same trend.

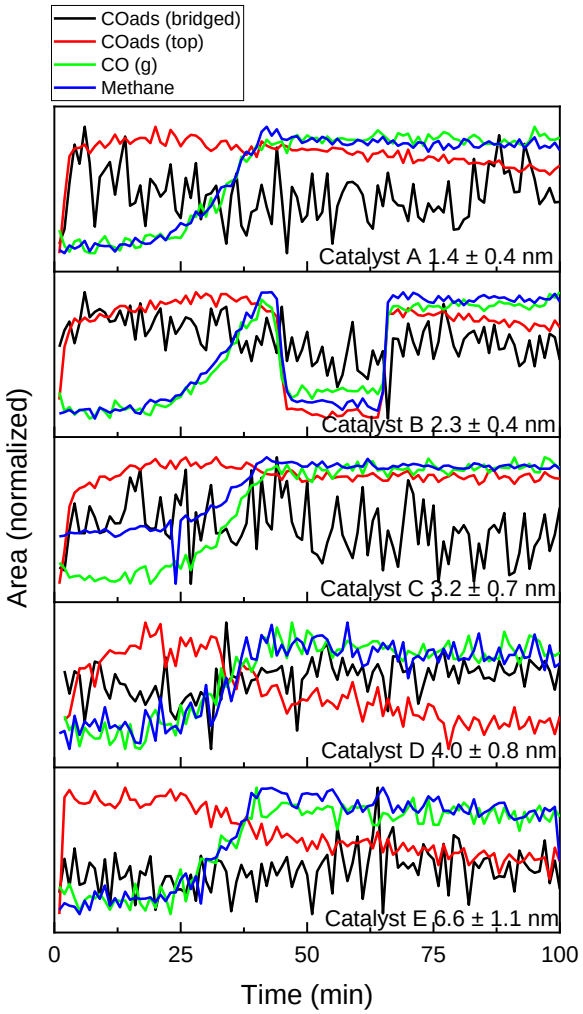

Figure SI 9 Integrated FT-IR peak areas of CO (g), COads (top), COads (bridged) and methane plotted versus time (normalized).

9. References

(1) Matsoukas, T.; Gulari, E. Dynamics of Growth of Silica Particles from Ammonia-Catalyzed Hydrolysis of Tetra-Ethyl-Orthosilicate. *J. Colloid Interface Sci.* **1988**, *124*, 252–261.

(2) Malay, O.; Yilgor, I.; Menceloglu, Y. Z. Effects of Solvent on TEOS Hydrolysis Kinetics and Silica Particle Size under Basic Conditions. *J. Sol-Gel Sci. Technol.* **2013**, *67*, 351–361.

(3) Yang, T. H.; Shi, Y.; Janssen, A.; Xia, Y. Surface Capping Agents and Their Roles in Shape-Controlled Synthesis of Colloidal Metal Nanocrystals. *Angew. Chemie Int. Ed.* **2020**, *59*, 15378–15401.

(4) Sun, C.; Ron, J.; Simke, J.; Gradzielski, M. An Efficient Synthetic Strategy for Ligand-Free Upconversion Nanoparticles. *Mater. Adv.* **2020**, *1*, 1602–1607.

Acknowledgements

Firstly, I want to thank Bram for his supervision. Thank you for your flexibility, open-mindedness and positive feedback and suggestions you gave. Thank you for improving my presentation and writing skills. Thank you, especially for your enormous patience during the project, from which I learned a lot.

Matteo, thank you for your encouragement during the meetings and valuable feedback. Your knowledge and ideas have inspired me.

Ward, thank you for your valuable feedback during the meetings and for being my examiner.

I would also like to thank Angela, Huygen, Mirjam, Joyce, Sofie, and Bettina for instructions with equipment, helping in the lab, and being my extra supervisor when Bram was unavailable.

Last, my wife Ebru, thank you for being beside me.